MAE--304

COUETTE FLOWS OF A GRANULAR MONOLAYER - AN EXPERIMENTAL STUDY

DE-FG22-91PC 91297

Kenneth E. Elliott, Goodarz Ahmadi and William Kvasnak

Department of
Mechanical and Aeronautical Engineering
Clarkson University
Potsdam, NY 13699-5725

Report No. MAE-304
March 1995

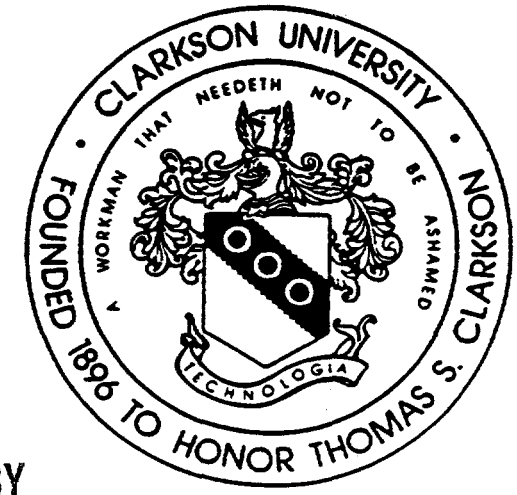

DISCLAIMER

Portions of this document may be illegible in electronic image products. Images are produced from the best available original document.

MAE--304

COUETTE FLOWS OF A GRANULAR MONOLAYER – AN EXPERIMENTAL STUDY

Kenneth E. Elliott, Goodarz Ahmadi, and William Kvasnak
Department of Mechanical and Aeronautical Engineering
Clarkson University, Potsdam, NY 13699-5725

ABSTRACT

An experimental study concerning rapid flows of granular materials in a two dimensional planar granular Couette flow apparatus is performed. The device is capable of generating particulate flows in grain-inertia regime at different shearing rates and solid volume fractions. Multi-color spherical glass particles are sheared across an annular test-section for several wall angular velocities. A video recorder is used to record the motion of particles, and consecutive images are stored and analyzed by an image processing technique for evaluating individual grain velocities. Experimental data for the mean velocity, the root mean-square fluctuation velocity components and the solid volume fraction profile are obtained. The resulting mean velocity profiles have a roughly linear variation for the range of solid volume fractions and shear rates studied. The solid volume fraction profiles exhibit nonuniform variations with the highest concentration occuring near the center of the shearing cell. The RMS-fluctuation velocities are roughly constant, with the streamwise fluctuation being somewhat larger than the cross-stream direction. The experimentally measured flow properties are in reasonable agreement with the earlier theoretical and simulation results.

INTRODUCTION

Understanding particulate transport processes is of crucial interest to the further development of environmentally acceptable coal energy systems. For example, improving the performance of advanced pressurized fluidized bed combustor and coal gasification requires a detailed knowledge of particulate flows. The flow behavior of relatively dense coal slurries and bulk solids in various complex geometry passages are indispensable to the economical design of coal energy conversion equipment. Because of its numerous industrial applications, there have been a number of studies concerning the mechanics of rapid flows of granular materials. Bagnold [1] was the first to perform a number of experiments using neutrally buoyant particles in a Couette flow device. He showed that both the shear and normal stresses vary as the square of the shear rate. Blinowski [2], Ogawa [3], and Ogawa et al. [4] recognized the importance of the velocity fluctuations in granular flows. Application of turbulence modeling approach to rapid flows of granular materials was reported by Blinowski [2] and Ahmadi and co-workers [5-7].

In the last decade, there has been considerable interest in developing a kinetic theory for modeling rapid granular flows. Developments in the kinetic formulation for particulate materials were reported by Jenkins & Savage [8], Ahmadi & Shahinpoor [9], Lun et al. [10], Jenkins & Richman [11] and Ahmadi & Ma [12]. A similar physical model was developed by Haff [13], and Savage [14], and Massoudi & Boyle [15] provided extensive reviews of the earlier kinetic and continuum model. Recently, Ma & Ahmadi [16] reported a new method for including the effects of interstitial fluid in their kinetic model, and Abu-Zaid & Ahmadi [17] developed a simple kinetic model for granular flows in grain-inertia regime including energy losses due to frictional slip during collision. Richman [18], and Ahmadi & Abu-Zaid [19] also proposed models for rapid granular flows that are capable of predicting the normal stress differences which are observed during rapid shearing of granular assembly.

Experimental studies of granular flows are rather scarce and are, generally, restricted to bulk flow measurements. Experimental data concerning variation of bulk shear and normal stresses with shear rate and solid volume fraction were reported

by Savage & McKeown [20], Savage & Sayed [21] and Hanes & Inman [22]. Experimental studies of granular gravity flows down an inclined chute were reported by Savage [23], Hungr and Morgenstern [24], Patton et al. [25] and Drake & Shreve [26], and Johnson et al. [27]. Flows of a collection of circular disks on an inclined air table was studied by Sanders et al. [28]. The study of Drake & Shreve [26] is most relevent to the present study since they measured individual grain velocities for steady gravity flows in an encapsulated two-dimensional chute.

The purpose of this work is to provide detailed experimental information concerning rapid shearing of granular flows. Two dimensional flows of glass particles in a Couette flow apparatus are studied. A digital image processing procedure is used to measure the instantaneous velocities and concentrations of particles for various solid volume fractions and shearing rates. Using an averaging technique, experimental data for variations of granular mean velocity, root-mean-square (RMS) fluctuating velocities, and solid volume fraction across the shearing cell are obtained. The resulting mean and RMS fluctuation velocity profiles, as well as the solid volume fraction are compared with earlier model predictions and discussed.

EXPERIMENTAL APPARATUS

In this section the experimental setup used in this study, including the Couette device and the image processing system are described.

A mono-granular shear flow apparatus is designed and fabricated. The cross section of the shearing cell and the Couette flow device are shown schematically in figure 1. The particles used in the experiment are glass marbles of different colors with a diameter of $d = 12\ mm$, a density of $\rho = 2.947\ g/cm^3$ and a restitution coefficient of $r = 0.95$. Figure 1a shows a schematic of the particles in the shearing cell. The inner and outer walls of the cell rotate in opposite directions, while the upper and lower walls are stationary. All walls are made of plexiglass so that the motion of granules could be monitored. The spacing between the inner and outer walls is 72 mm which is equivalent to six particle diameters, while the distance between the upper and lower walls is only 13 mm which is somewhat larger than

the particle diameter. This configuration allows the particles to be sheared while forming a roughly mono-granular layer. In order to increase the friction between the particles and the rotating walls of the shearing cell, the inner and outer walls are roughened by attaching toothed rubber belting.

The cylindrical Couette geometry used generates a steady simple shear particulate flow. A series of gears and pulleys, and two timing belts enable a single motor to drive the inner and the outer walls of the shearing cell in opposite directions. Figure 1b shows a schematic of the cross-section of the apparatus used to drive the inner and outer walls of the shearing cell. Figure 2 is a photograph of the shear flow setup. Additional details of the Couette flow apparatus were given by Elliott [29].

A video camera which records 30 frames per second is used to record several minutes of the granular flow under various conditions. A single incandescent lamp is used to illuminate the test section of the shearing cell. A VCR with single frame advance feature is used in conjunction with a PC based true color image processing system to store and analyze consecutive images. The coordinates of each particle on the image were mapped between two consecutive frames, and used to evaluate the instantaneous position and velocity of the granules.

EXPERIMENTAL PROCEDURE

In this section the procedure for the experimental study is outlined and the method for analyzing images is discussed. The averaging techniques for velocity and solid volume fraction are also described.

The camera was set up vertically and was focused onto the test section of the shearing cell. The size of the test section was 170 x 72 *mm*. A shutter speed of 1/1000 *sec* was used to ensure an accurate image of each particle. Due to the encapsulation of the mono-granular layer in the Couette flow device, the particles were forced to remain in the focal plane and behave essentially as disks. The mean solid volume fractions were initially estimated as a function of the maximum packing factor (MPF) allowed by the geometry of the setup. Here, the MPF is defined as the ratio of the area of the maximum number of particles which can occupy a specific

area, to the total area. For an unbounded region, the maximum packing factor for disks (or spheres in a two-dimensional configuration) is 0.907. For the experimental shear cell configuration (the annulus between the inner and the outer cylinders) the maximum packing factor was 0.8313. Using the estimated value for the MPF, the number of particles required for bulk surface fractions of roughly 20 % to 60 % were introduced in the shearing cell. The Couette flow apparatus was then turned on and a stop watch was used to determine the approximate rpm of the outer wall. The exact speed of the outer wall was later determined from the displacement of the screws which affixed the outer wall, on the video images. After two to three minutes when the granular flow had reached the steady state, the camera was switched on for over two minutes (3600 frames). For a fixed mean surface fraction, $\overline{\nu}_{2D}$, the experimental data were obtained for a range of speeds up to 75 *rpm.*

The recorded color frames were then analyzed by a digital image processing technique. Two consecutive frames were digitized using 640 by 480 pixel resolution and stored. Figure 3 shows two consecutive frames for a mean surface fraction $\overline{\nu}_{2D}$ of 23% and rotational speed of 60 *rpm.* These pictures illustrate the nonuniformity of the velocity across the shear cell. The particles near the center of the flow have nearly zero velocity. Particles adjacent to the inner and the outer walls, however, have a much higher velocity.

The positions of the center of each particle on the screen are identified. The coordinates x_{1j} and y_{1j} of particles from frame 1 were recorded, and mapped to frame 2 where their new coordinates were recorded as x_{2j} and y_{2j}. The video tape was then advanced five to six frames to insure that the next two frames used were independent of the previous samples. Frames were continuously viewed and particle positions were recorded until 1860 grains were mapped. Particle positions were recorded in pixels, and then converted into physical coordinates. (For the condition of the experiment, there were 30 *pixels* per *cm.*)

The velocities of individual particles and the concentration profile of the flow were then evaluated from the locations of the sphere centers on successive frames. The control volume of the shearing cell is broken into 9 overlapping equal width bins

as shown in figure 4, and each particle was placed into a bin based on its centroid y_{1j} or r_{1j} coordinates. Particle velocities (U, V) and/or (V_r, V_θ) are described in relation to the Cartesian (x, y), as well as the polar (r, θ) coordinate system were evaluated. The instantaneous velocity of the "j^{th}" particle was estimated as

$$u_j = \frac{(x_{2j} - x_{1j})}{1/30 sec}, \tag{1}$$

where x_{2j} and x_{1j} are the respective x coordinates of particle "j" mapped from frame 1 to frame 2, and $1/30$ sec is the time difference of exposure between successive frames. The average velocities were then computed for each bin (i = 1,2,3...,9) across the test-section according to

$$U^{(i)} = \frac{1}{N_{pi}} \sum_{j=1}^{N_{pi}} u_j, \tag{2}$$

where N_{p_i} is the number of particles in each bin summed over all pairs of consecutive frames. The transverse instantaneous velocity v_j and the average $V^{(i)}$ velocity for each bin were computed in exactly the same manner using y_{2j} and y_{1j} as the respective particle coordinates.

Once the average $U^{(i)}$ and $V^{(i)}$ velocities were determined for each bin, their respective root-mean-square velocities were estimated by

$$u'^{(i)} = \sqrt{\frac{1}{N_{pi}} \sum_{j=1}^{N_{pi}} \left(u_j^{(i)} - U^{(i)}\right)^2} \quad and \quad v'^{(i)} = \sqrt{\frac{1}{N_{pi}} \sum_{j=1}^{N_{pi}} \left(v_j^{(i)} - V^{(i)}\right)^2}. \tag{3}$$

The average fluctuation kinetic energy for each bin was calculated using the expression

$$k^{(i)} = \frac{1}{2} \left(u'^{(i)2} + v'^{(i)2}\right). \tag{4}$$

An error analysis for the technique used is described in Appendix A.

Since the walls of the shearing cell are moving in opposite directions, the ideal shear rate is given as

$$\dot{\gamma}^I = \frac{\mid u_{outer} \mid + \mid u_{inner} \mid}{H} \tag{5}$$

where H is the width of the annulus. The effective (actual) shear rate, however, is much lower than the ideal one due to the presence of a significant level of slip at the

wall. A slip velocity is defined as the difference between the wall velocity and the average particle velocity in the bin adjacent to the (inner or the outer) wall, i.e.,

$$u_{slip} = u_{wall} - U^{(i)} \quad for \;\; i = 1 \;\; or \;\; 9. \tag{6}$$

The effective shear rate is then defined as

$$\dot{\gamma} = \frac{\mid U^9 \mid + \mid U^1 \mid}{H}, \tag{7}$$

which is the shearing rate experienced by the bulk of the granular layer.

The particles may traverse a nominal distance of about 2 mm in the z-direction equivalent to one-sixth of their diameter, however, they are unable to ride atop of one another. The two-dimensional solid surface fractions for the experiments may then be converted to three-dimensional solid volume fractions by incorporating the volume allowed for the particles to move. The average three-dimensional solid volume fraction (solids concentration) $\overline{\nu}_{3D}$, and the two dimensional surface fraction $\overline{\nu}_{2D}$, was determined for each experimental Couette flow condition as

$$\overline{\nu}_{3D} = \frac{\pi d^3}{6\mathcal{V}} \frac{N_{total}}{N_f}, \quad \overline{\nu}_{2D} = \frac{\pi d^2}{4\mathcal{A}} \frac{N_{total}}{N_f}, \tag{8}$$

where the subscript $3D$ and $2D$ correspond to three dimensional volume or two dimensional surface fraction, respectively. Here $\mathcal{V}$ = 17.0 x 7.2 x 1.38 cm^3 is the total volume of the shear cell test-section, $\mathcal{A}$ = 17.0 x 7.2 cm^2 is the total area and N_{total} represents the total number of particles mapped for N_f frames for a specific flow. The average solid volume (surface) fraction of particles in bin "i" was evaluated as

$$\nu_{3D}^{(i)} = \frac{N_{pi}}{N_f} \frac{\pi d^3}{6\mathcal{V}^{(i)}} \quad and \quad \nu_{2D}^{(i)} = \frac{N_{pi}}{N_f} \frac{\pi d^2}{4\mathcal{A}^{(i)}}, \tag{9}$$

where $\mathcal{V}^{(i)}$ = 17.0 x 1.44 x 1.38 cm^3 is the volume of one bin and $\mathcal{A}^{(i)}$ = 17.0 x 1.44 cm^2 is the surface area of one bin. A linear concentration parameter s was defined by Bagnold [1] as the average distance between the outer surfaces of particle pairs within the flow. The linear concentration can be evaluated for two and three dimensional configurations as

$$s_{2D} = d\left(\sqrt{\nu_{2DM}/\overline{\nu}_{2D}} - 1\right) \quad and \quad s_{3D} = d\left(\sqrt[3]{\nu_{3DM}/\overline{\nu}_{3D}} - 1\right) \tag{10}$$

Table 1: Solid Volume Fractions, Wall Angular Velocities and Frames Studied

Speed (rpm)	ν 0.18	ν 0.23	ν 0.36	ν 0.46	ν 0.54
45			X	X	X
60		X	X	X	
75	X		X		
Frames	200	160	100	80	72

where $\nu_{2DM} = 0.907$ and $\nu_{3DM} = 0.74$ are the maximum packing for spheres.

The actual mean two-dimensional surface fractions as defined by equation (8) used in the experiment were 18%, 23%, 36%, 46% and 54%. The corresponding three-dimensional solid volume fractions were, respectively 9.8%, 12.6%, 19.7%, 25.1% and 29.5%. A table of the experimental conditions is given in Table 1.

EXPERIMENTAL RESULTS

The experimental data for a range of solid volume fractions and shear rates are compiled and the results are described. in this section.

Figures 5 through 11 show the experimental data for the mean and the root-mean-square velocity components, and the concentration profiles for different mean solid volume fractions and shear rates in the shear cell. The solid lines in these figures correspond to the least square error fit to the data. Here, the distances are measured from the outer wall.

Figure 5 shows the results for a relatively dilute case with $\overline{\nu}_{3D} = 9.8\%$ ($\overline{\nu}_{2D} = 18\%$) and an effective shear rate of 4 sec^{-1}. For this case the ideal shear rate (based on the speed of the inner and outer walls) was $\dot{\gamma}^I = 74.8\ sec^{-1}$. The streamwise velocity profile (U) across the test-section, is linear with the maximum mean particle velocities occurring at the outer wall. This observation shows that the Couette flow device generates a simple shear flow condition with reasonable accuracy. Although the wall velocities for the flow are 298 cm/sec at the outer wall and 241 cm/sec

at the inner wall (for a running speed of 75 rpm), the largest streamwise velocity measured is 16.4 cm/sec. This implies that slip velocities of 281 cm/sec at the outer wall and 229 cm/sec at the inner wall exist. The large magnitude of the slip velocity may be attributed to a low value of wall roughness, the relatively fast moving wall and a small solid concentration. At such a small solid volume fraction, each particle is allowed to travel further before interacting with another particle. The average distance between particle pairs for this flow is 1.5 cm (approximately 1.25 times the particle diameter). With this spacing the particles are not forced to stay against the rapidly moving boundaries, and hence, an extremly large amount of slip occurs.

The data points for the cross-stream (V) component of velocity are also shown in figure 5a. At steady state the mean cross-stream velocity is expected to be zero across the annulus. The scatter of the data is in part due to the effect of the annular shape of the shearing cell, and the fact that the outer cylinder moves with a higher velocity, as well as the inherent experimental error.

Figure 5b shows that the average root-mean-square (RMS) velocities are about fifty percent of the peak mean velocity and are nearly constant across the shear cell. The solid volume fraction shown in figure 5c has a roughly parabolic profile with the largest solids concentration occurring between the centerline and the inner cylinder.

Figure 6 shows the results for a mean solid volume fraction of $\overline{\nu}_{3D} = 12.6\%$ ($\overline{\nu}_{2D} = 23\%$) and an effective shear rate of 7.9 sec^{-1} with $\dot{\gamma}^I = 59.9\ sec^{-1}$. In this case the outer and the inner wall of the shear cell were moving at 238 and 193 cm/sec, respectively (for a running speed of 60 rpm). Figure 6a shows a roughly linear trend for the U-component of velocity across the annulus. The observed slip velocities are 206 cm/sec at the outer wall and 170 cm/sec at the inner wall. It is observed that the slip velocities are reduced as the mean solid volume fraction increases. As the number of particles within the shear cell is increased, the distance between particle pairs decreases. The average distance between particles for this granular flow was estimated as 1.2 cm. The maximum U velocity of 32.5 cm/sec is approximately twice that of the previous case where the effective shear rate was 4 sec^{-1}. Figure 6a shows that the V-component of the velocity fluctuates slightly around the zero-level.

The RMS fluctuation velocities shown in figure 6b exhibit a nearly constant trend. Between the center of the cell and the outer wall, the axial fluctuation velocity u', exceeds slightly over the v' component. Figure 6c shows the solid volume fraction profile. The profile is more uniform when compared to the previous case, and varies from a minimum of 0.11 at the outer wall to a maximum of 0.14 near the center.

Figures 7-9 show the experimental data for a mean solid volume fraction $\overline{\nu}_{3D}$ of 19.7% ($\overline{\nu}_{2D} = 36\%$) and effective shear rates of 6.9, 8.8 and 15.6 sec^{-1}, respectively. The wall angular velocities for an effective shear rate of 6.9 sec^{-1} were 179 cm/sec at the outer wall and 145 cm/sec at the inner wall corresponding to a running speed of 45 rpm. The average interparticle distance, $s_{2D} = 0.7$ cm, is the same for these three cases. The streamwise velocity profiles across the annulus are linear, and comparison of the measured maximum mean velocities at the outer wall shows an increase from 30 cm/sec for $\dot{\gamma} = 6.9$ sec^{-1} to 80 cm/sec for $\dot{\gamma} = 15.6$ sec^{-1}.

The slip velocities at the outer wall are still quite large, 149 cm/sec for $\dot{\gamma} = 6.9$ sec^{-1}, 198 cm/sec for $\dot{\gamma} = 8.8$ sec^{-1} (on the order of five times the particle near wall velocity) and 218 cm/sec for $\dot{\gamma} = 15.6$ sec^{-1} (roughly three times the particle near wall velocity). At the inner cylinder, the magnitude of the slip velocity for $\dot{\gamma} = 8.8$ sec^{-1} is 172 cm/sec (approximately nine times the particle near wall velocity) and for $\dot{\gamma} = 15.6$ sec^{-1}, $u_{slip} = 208$ cm/sec (roughly six times the particle near wall velocity). The slip velocities for the outer and inner cylinders increase with increasing shear rate. The location of the zero streamwise velocity is roughly at the center of the test-section for $\dot{\gamma} = 6.9$ sec^{-1} and shifts toward the inner wall at higher shear rates. This shift which could reach to approximately one-seventh of the shearing cell width is attributed to a higher tangential velocity of the particles adjacent to the outer wall.

The cross-stream velocity component in figures 7a, 8a, and 9a show scattered about the zero-level with a slightly positive trend near the outer cylinder and a slightly negative trend near the inner cylinder. This implies that there is tendency for particles to move away from the rapidly moving walls.

The root-mean-square velocities u' and v' shown in figures 7b, 8b, and 9b show significant levels of velocity fluctuations. It is also observed that the magnitude of u' and v' are, generally, comparable with the axial fluctuation exceeding the lateral one at higher shear rates. This trend is more obvious in the region near the outer wall. The solid volume fraction profiles vary across the shear cell and range from 0.12 at the outer wall to 0.22 at the center. As shear rate increases, the solid volume profile tends to become more uniform.

Figure 10 shows the experimental results for a mean solid volume fraction of $\overline{\nu}_{3D}$ = 25.1% ($\overline{\nu}_{2D}$ = 46%) and an effective shear rates of 10 sec^{-1} (with wall angular velocity of 45 rpm). Here, the average distance between particle pairs for is 0.49 cm. The streamwise velocity profile across the test-section in figure 10a is roughly linear with its maximum of 47 cm/sec occurring at the outer wall. The mean velocity adjacent to the inner wall is 26 cm/sec in this case. The slip velocity at the outer cylinder is 132 cm/sec (of the order of three times the particle near wall velocity). At the inner cylinder a slip velocity of 119 cm/sec (about five times the particle near wall velocity) is observed. The mean cross-stream velocities in figure 10a is approximately zero across the annulus. Figure 10b shows that the RMS fluctuation velocity profiles are nearly constant across the annulus, and have comparable magnitudes. The solid volume fraction varies from 0.17 at the outer cylinder to 0.27 near the center of the shear cell.

Figure 11 shows the experimental data for a mean solid volume fraction $\overline{\nu}_{3D}$ of 29.5% ($\overline{\nu}_{2D}$ = 54%) and a shear rate of 9.7 sec^{-1}. The average particle-particle distance is 0.355 cm or approximately one-third of the particle diameter. The concentration of 0.29 was the highest mean solid volume fraction studied. The streamwise velocity profile is roughly linear across the shear cell with a maximum velocity of 45 cm/sec occurring at the outer wall. The slip velocities of 133.5 and 119.6 cm/sec at the outer and the inner walls for this flow are comparable to the values of 131.8 and 118.8 cm/sec estimated for the case of $\overline{\nu}_{3D}$ = 0.25 and $\dot{\gamma}$ = 10 in figure 10a. (The effective shear rates between these two cases were only marginally different.) This further shows that the slip velocities predominantly depend on the shear rate.

The root-mean-square velocity profiles of figure 11b show some scatter across the shear cell, being slightly lower near the annulus center when compared to the boundaries. The axial fluctuation velocity u' seems to exceed the v'-component in the region near the outer cylinder. The solid volume fraction profile in figure 11c shows that peak concentration is shifted towards the inner cylinder.

The mean streamwise velocities for each bin across the annulus were non - dimensionalized with aid of the maximum velocity for each flow. (The largest mean particle velocities always occurred in the bin adjacent to the outer wall). Figure 12a shows the variations of non-dimensional mean velocities U/U_{max} versus non-dimensional distance Y/H for a constant solid volume fraction of $\nu_{3D} = 0.2$ and different shear rates. Similarly, variations are shown in figure 12b, where ν is varied and $\dot{\gamma}$ is roughly constant ($7.9\ sec^{-1} \leq \dot{\gamma} \leq 9.7\ sec^{-1}$). It is observed that the mean velocity profiles exhibit roughly linear characteristics across the test-section. Figure 12a shows that as $\dot{\gamma}$ increases, the non-dimensional velocity near the inner wall decreases. A similar trend is noticed from figure 12b when ν increases for a roughly constant shear rate.

Figure 13a shows variations of slip velocity with particle concentration for a roughly fixed shear rate of $7.9\ sec^{-1} \leq \dot{\gamma} \leq 9.7\ sec^{-1}$. This figure shows that the slip velocity decreases as the solid volume fraction increases. This behavior is consistent with the classical gas dynamics, for which, at normal concentration, no slip occurs, while the rarefied gas experiences a significant amount of slip. Figure 13b shows the variation of slip velocity with shear rate for a fixed solid volume fraction of $\nu_{3D} = 0.2$. The least amount of slip occurs for an effective shear rate of $9.7\ sec^{-1}$ (with wall angular velocities of 30 rpm). This figure also shows the expected trend that the slip velocity increases as the effective shear rate increases. The significant amount of slip velocity observed in this experiment is due to the low wall roughness of the shearing cell.

COMPARISONS

In this section the present experimental data are compared with the earlier the-

oretical and computer simulation models.

Figure 14 shows a comparison of the measured non-dimensional velocity U/U_{max}, and fluctuation kinetic energy for an effective shear rate of $\dot{\gamma} = 9.7sec^{-1}$ with the numerical simulation results of Abu-Zaid & Ahmadi [17] and Campbell & Brennen [30] for a mean surface fraction of 0.54. In this figure, the outer and/or inner wall data corresponds to the velocity field between the point of zero-velocity and the outer and/or inner wall of the shearing cell. The solid line, which is the least-square-fit to the experimental data for the non-dimensional streamwise velocity component U/U_{max} shows the same qualitative trend as the earlier simulation results. The average fluctuation kinetic energy profile is also consistent with the results of Abu-Zaid & Ahmadi, but somewhat larger than those predicted by Campbell & Brennen. Although slight discrepancies exist, the present experimental data are in general agreement with the model prediction of Abu-Zaid & Ahmadi and the molecular dynamic simulation of Campbell & Brennen.

The non-dimensional ratio of the mean shear rate to the root-mean-square fluctuation energy, R, defined as

$$R \equiv \frac{d\dot{\gamma}}{\sqrt{2k}}, \tag{11}$$

has been used in many earlier theories for granular flows. In Appendix B, the theoretical expressions for the parameter R are summarized. Here, a comparison of the experimental data for R with the theoretical values is presented. For a restitution coefficient of $r = 0.95$ for glass beads, figure 15 shows the variation of R with solid volume fraction according to different theories. Here, $\nu_m = 0.64356$ (corresponding to the maximum solid volume fraction for which shearing flow is possible), was used for the theories of Ogawa *et al.* [4] and Shen & Ackermann [31]. (In their original models, $\nu_m = 0.707$, was suggested.) The present experimental data, which are limited to solid volume fractions ranging from 0.1 to 0.3, are shown in figure 15 for comparison. The values for R are evaluated from the effective shear rate of each flow, and the average fluctuation energy across the shearing cell. It is observed that R increases with ν at the low solid volume fraction, and approaches a constant value at the high concentrations. The exception is the model of Jenkins & Savage

which predicts values for R that are independent of ν. The theory of Abu-Zaid & Ahmadi shows that as μ increases the value of R increases. The prediction of Lun *et al.* gives the lowest values of R for small solids fractions, while that of Ogawa *et al.* leads to the highest value (about twice those of the other model predictions). The present data shows the increase of R with ν and exhibits the same trend as the model predictions. In particular, the present data seems to agree with the prediction of Abu-Zaid & Ahmadi for a friction coefficient of $\mu = 0.01$.

Figure 16 compares the present data for variation of non-dimensional kinetic normal stress component τ_{22}^{k} with the parameter R as predicted by various available models for the case of simple shear flow. Here, a value of $\nu_m = 0.64356$ and ν =0.29 were used. The model predictions show that the non-dimensional normal stress component decreases with increasing R. For small R, the non-dimensional normal stress varies as R^{-2}, while for large R, the non-dimensional normal stress component approaches a constant value. Savage & Jeffrey [32] discussed this behavior for all values of R. The limit $R \rightarrow 0$ is equivalent to the case where the mean shear characteristic velocity $\rho \mid du/dy \mid$ tends to zero with the fluctuation velocity $(\overline{v'^2})^{\frac{1}{2}}$ fixed. When the fluctuation velocity $(\overline{v'^2})^{\frac{1}{2}}$ tends toward zero, R becomes very large. For the present study, R ranged from 0.3 to 0.5, and the experimental data for the non-dimensional kinetic normal stress decreases with increasing R analogously to the model predictions. The rate of decrease is faster than the model predictions, however, because the experimental data only includes the kinetic part of the normal stress, while the model predictions are for total (kinetic *and* collisional) normal stresses.

Figures 17 and 18 compare the present experimental data for the root-mean-square velocity components with the model predictions of Abu-Zaid & Ahmadi [33]. A value of $r = 0.95$ for glass beads, and the mean values of the effective experimental shear rates and solid volume fractions are used in the model. The solid and dashed lines in these figures correspond to u' and v', respectively, as predicted by the model. Figure 17a shows the root-mean-square (RMS) velocity data for the solid volume fraction of 9.8% and an effective shear rate of 4 sec^{-1}. The theoretical solutions

predict slightly smaller values for the root-mean-square velocity components for this case. Figure 17b shows the experimental data and the theoretical results for the RMS velocity components for a solid volume fraction of 12.6% and an effective shear rate of 7.9 sec^{-1}. The experimental data for v' is in excellent agreement with the theoretical predictions across the shear cell. The data for u' at the outer wall, however, is somewhat higher than the model prediction. Figures 17c, 17d and 18a show the RMS velocities for a solid volume fraction of 19.7% and effective shear rates of 6.9, 8.8 and 15.6 sec^{-1}, respectively. Although some scatter exists, general agreement between the experimental data and the model predictions is reasonable.

Figures 18b and 18c show the comparison for a solid volume fraction of 25.1% and respective effective shear rates of 10.0 and 11.5 sec^{-1}. The model predictions appear to overpredict the experimental data. Figure 18d shows the results for the largest solid volume fraction of 29.5% studied. The effective shear rate for this case was 9.7 sec^{-1}. From figures 17 and 18, it is observed that both the model predictions and the experimental data for the RMS axial fluctuation velocity are somewhat larger than those for the transverse component. This provides further proof on the anisotropic nature of kinetic stresses in rapid granular flows. These figures also show that the model predicts quite accurately the magnitude of the fluctuation velocities at low shear rates (less than 9 sec^{-1}). At higher shear rates, however, the theoretical predictions for the root-mean-square velocities are somewhat larger than the experimental data.

CONCLUSIONS

An experimental mono-granular shear flow device is designed, constructed, and is used to acquire data for velocity, concentration and root-mean-square fluctuation velocity profiles for various shear rates and solid volume fractions. The data is statistically analyzed and compared with the earlier theoretical model predictions for rapid granular simple shear flows. Profiles of the mean and the root-mean square velocities, as well as, solid volume fractions are evaluated for various mean solids concentrations and effective shear rates. Based on the presented results, the follow-

ing conclusions may be drawn:

1. The mono-granular Couette flow device and the video-image analysis procedure provides a viable method for studying rapid granular flows.

2. For non-dilute concentrations, steady and uniform granular simple shear flows are found to occur for various concentrations and shear rates. In each case the flow is characterized by a roughly linear mean velocity, and an approximately constant root-mean-sqaure velocity component profile.

3. Concentrations reported in this study covers the solids surface fraction in the range of 18% to 54%. For a ν_{2D} less than 18%, a steady state condition could not be achieved (in a reasonable amount of time) at a wall velocity of 75 rpm due to the lack of sufficient number of collisions between the particles. Above the solid surface fraction of 54% the particles may exhibit solid characteristics and are not sheared across the entire annulus.

4. All flows exhibited a nearly linear velocity profile across the test-section, with the largest velocities occurring at the outer wall, and the root-mean-square velocities showing a roughly constant trend. Solid volume fraction profiles exhibited a roughly convex variation across the test-section, with the highest concentration occuring at the center of the shearing cell. This observation shows that the Couette flow apparatus generates a simple shear flow condition with reasonable accuracy.

5. The experimental data show a significant amount of slip at the wall due to the relative small amount of wall roughness. The slip at the outer wall (which has the higher velocity) is always larger than that at the inner wall.

6. For a constant shear rate, the slip velocity is found to decrease as the solid volume fraction increases. Likewise, for a fixed solid volume fraction, the slip velocity increases with shear rate.

7. The experimental data for the RMS fluctuation velocity components show the anisotropy of the kinetic stresses during rapid granular flows.

8. The experimentally measured velocity and fluctuation kinetic energy profiles (for a solid surface fraction of 54%) show good agreement with the earlier theoretical predictions.

9. The measured values of the ratio of the mean effective shear rate to the square root of the particle fluctuation energy, R, as a function of the coefficient of restitution, solid volume fraction, and normal stress are in reasonable agreement with the earlier model predictions.

10. The experimental root-mean-square fluctuation velocity components are shown to be in qualitative agreement with the model predictions of Abu-Zaid & Ahmadi.

Acknowledgment

The financial supports of the US Department of Energy (University Coal Research Program, PETC) through Grant No. DE-FG22-94PC94213 is gratefully acknowledged.

REFERENCES

1. Bagnold, R.A., Experiments on a gravity-free dispersion of large solid spheres in a Newtonian fluid under shear. Proc. Roy. Soc. London A225, 49-63 (1954).

2. Blinowski, A., On the dynamics of granular media. Arch. Mech. 30 27-34 (1979).

3. Ogawa, S., Multitemperature theory of granular materials. Proc. US-Japan Seminar on Continuum-Mechanical and Statistical Approaches in the Mechanics of Granular Materials, 208-217 (1978).

4. Ogawa, S., Unemura, A. and Oshima, N., On the equations of fully fluidized granular materials. ZAMP 31, 483-493 (1980).

5. Ahmadi, G. and Shahinpoor, M., Towards a turbulent modeling of rapid flow of granular materials. Pow. Tech. 35, 241-248 (1983).

6. Ahmadi, G., A turbulence model for rapid flows of granular materials, Part I. Basic theory. Pow. Tech. 44, 261-268 (1985).

7. Ma, D. and Ahmadi, G., A turbulence model for rapid flows of granular materials, Part II. Simple shear flows. Pow. Tech. 44, 269-279 (1985).

8. Jenkins, J.T. and Savage, S.B., A theory for the rapid flow of identical, smooth, nearly elastic particles. J. Fluid Mech. 130, 187-202 (1983).

9. Ahmadi, G. and Shahinpoor, M., A kinetic model for rapid flow of granular materials. Int. J. Nonlinear Mech. 19, 177-186 (1983).

10. Lun, C.K.K., Savage, S.B., Jeffrey, D.J. and Chepurnity, N., Kinetic theories for granular flow: Inelastic particles in Couette flow and slightly inelastic particles in a general flow field. J. Fluid Mech. 140, 223-256 (1984).

11. Jenkins, J.T. and Richman, M.W., Grad's 13-moment system for a dense gas of inelastic spheres. Arch. Rational Mech. Anal. 87, 355-377 (1985).

12. Ahmadi, G. and Ma, D., A kinetic model for granular flows of nearly elastic particles in grain-inertia regime. Int. J. Bulk Solids Storage in Silos 2, 8-16, (1986).

13. Haff, P.K., Grain flow as a fluid-mechanical phenomena. J. Fluid Mech. 134, 401-430 (1983).

14. Savage, S.B., The mechanics of rapid granular flows. Adv. in Applied Mech. 24, 289-366 (1984).

15. Massoudi, M. and Boyle, E.J. A review of theories for granular materials with applications to fluidized beds and solid transport. Tech. Rep., DOE/PETC/TR-91/8, Pittsburgh, PA (1991).

16. Ma, D. and Ahmadi, G., An equation of state for dense rigid sphere gases. J. Chem. Phys. 84, 3449-3450 (1986).

17. Abu-Zaid, S. and Ahmadi, G., Analysis of rapid shear flows of granular materials by a kinetic model including frictional losses. Powder Technology, 77, 7-17, (1993).

18. Richman, M.W., Boundary conditions based upon a modified Maxwellian velocity distribution for flows of identical, smooth, nearly elastic spheres. Acta. Mech., 75, 227-240, (1988).

19. Ahmadi, G. and Abu-Zaid, S., A rate-dependent thermodynamical model for rapid granular flows. J. Non-Newtonian Fluid Mech. 35, 15-35, (1990).

20. Savage, S.B. and McKeown, S., Shear stresses developed during rapid shear of concentrated suspensions of large spherical particles between concentric cylinders. J. Fluid Mech., 127, 453-472, (1983).

21. Savage, S.B. and Sayed, M., Stresses developed by dry cohesionless granular materials in an annular shear cell. J. Fluid Mech., 142, 391-430, (1984).

22. Hanes, D.M. and Inman, D.L., Observations of rapidly flowing granular fluid flow. J. Fluid Mech., 150, 357-380, (1985).

23. Savage, S.B., Gravity flow of cohesionless granular materials in chutes and channels. J. Fluid Mech. 92, 53-96 (1979).

24. Hungr, O., and Morgenstern, N.R., Experiments on the flow behavior of granular material at high velocity in an open channel. Geotechnique, 34, 405-413, (1984).

25. Patton, J.S., Brennen, C.E. and Sabersky, R. H., Shear flows of rapidly deforming granular materials. ASME J. Appl. Mech., 54, 801-805, (1987).

26. Drake, T.G., and Shreve, R.L., High speed motion pictures of nearly steady, uniform, two-dimensional, inertial flows of granular materials. J. Rheology, 50, 981-993, (1986).

27. Johnson, P.C., Nott, P., and Jackson, R., Frictional-collisional equations of motions for particulate flows and their applications to chutes. J. Fluid Mech., 210, 510-535, (1990).

28. Sanders, B.E., Hopkins, M.A., and Ackermann, N.L., "Physical Experiments and Numerical Simulation of Two Dimensional Chute Flow. Micromechanics of Granular Materials", Satake, M. and Jenkins, J.T., eds., Elsevier, New York (1988).

29. Elliott, K.E., "Experimental Analysis of Granular Simple Shear Flows", Master Thesis, Clarkson University, Potsdam, NY (1994).

30. Campbell, C.S., and Brennen, C.E., Chute flows of granular material: some computer simulations. ASME J. Appl. Mech., 172, 172-178, (1985b).

31. Shen, H. and Ackermann, N.L., Constitutive relations for fluid-solid mixtures. J. Engng. Mech. Div. ASCE 108 748-763 (1982).

32. Savage, S.B., and Jeffrey, D.J., The stress tensor in a granular flow at high shear rates. J. Fluid Mech. 110, 255-272 (1981).

33. Abu-Zaid, S. and Ahmadi, G., Simple kinetic model for rapid granular flows including frictional losses. J. Engng. Mech. 116, 379-389 (1990).

34. Ackermann, N.L. and Shen, H., Stresses in rapidly sheared fluid-solid mixtures. J. Engng. Mech. Div. ASCE 108 95-113 (1982).

APPENDIX A: Error Analysis

The image analysis method used is associated with certain error due to the sampling frequency limitation of 1/30 *sec* of the video system. That is, if the mean time between collisions for a particle is less than 1/30 *sec*, the particle may undergo several collisions in the time duration between two consecutive frames. Thus, the present technique measures the time averaged particle velocity (over 1/30 *sec*). While this may not affect the mean particle velocity in a bin, it is substantially more important for the root-mean-sqaure (RMS) fluctuation velocity measurement in that it will filter out all of the fluctuation energy in the frequencies higher than 30 Hz.

The average time between collisions (inverse of collision frequency) is given as:

$$Average\ time\ between\ collisions \approx \frac{s_{2D}}{u'}, \tag{12}$$

where u' is the RMS fluctuation and s_{2D} is the average distance between particle pairs. Table 2 lists some typical mean times between successive collisions for different solid surface fractions and the number of collisions which occur in 1/30 *sec*. When the average time between collisions is greater than 1/30, the present measurement procedure provides a good assessment of the root-mean-square velocity. It is observed that for most surface fractions studied an accurate measurement of the fluctuation velocities is made. For higher concentrations, however, the present technique underestimates the intensity of particle fluctuation velocities to an extent.

The statistical error associated with the evaluations of the mean quantities (velocities and solid volume fractions) are on the order of

$$error \approx \frac{1}{\sqrt{1860/9}} \approx 0.07, \tag{13}$$

where 1860/9 is the total number of particles in one bin. There is also inherent error associated with the mapping technique, especially in determining the exact centroid of each particle. This "centering" error is approximately $\pm$ 1 pixel, or roughly 1/18 of the particle diameter. Error is also associated with the spatial resolution of the data due to the size of the bins used.

Table 2: Typical mean time between collisions and number of collisions occurring in 1/30 *sec*

Surface Fraction	s_{2D} (cm)	$\dot{\gamma}$ $(1/sec)$	u' (cm/sec)	s/u' (sec)	# of Collisions
0.18	1.5	4.0	8.0	$0.19 \approx 1/5$	0.18
0.23	1.2	7.9	14.3	$0.08 \approx 1/12$	0.40
0.36	0.7	6.9	9.1	$0.08 \approx 1/12$	0.43
0.36	0.7	8.8	13.5	$0.052 \approx 1/19$	0.58
0.36	0.7	15.6	24.5	$0.03 \approx 1/33$	1.16
0.46	0.49	10.0	11.6	$0.042 \approx 1/24$	0.80
0.46	0.49	11.5	14.3	$0.034 \approx 1/29$	0.98
0.54	0.36	9.7	11.7	$0.03 \approx 1/33$	1.10

APPENDIX B: Variation of Mean Shear Rate to Fluctuation Energy Ratio R with Solid Volume Fraction

Savage & Jeffrey [32] introduced the non-dimensional parameter R as the ratio of the characteristic mean shear rate to the root-mean-square of the particle fluctuation velocity. The parameter R is proportional to the ratio of the particle relative velocities due to the mean shear field and their random fluctuation (thermal) motions. For example, a value of R near 1 indicates that particles located one diameter apart have a relative velocity due to the mean shear field that is as large as their fluctuation velocities. The parameter R may also be interpreted as a microscopic granular Reynolds number. When R is small, the granular flows are dominated by the collisional momentum and energy transport, and the modern kinetic theories are applicable. In this appendix, the expressions for R as predicted by various models are presented.

The variation of R with solid volume fraction and coefficient of restitution were evaluated by several authors in the past. The more recent derivation of Abu-Zaid

& Ahmadi [33] includes the effects of frictional energy losses. i.e.,

$$R = f(\nu)\left[(1+r)\left(1-r+2\mu\right)\right]^{1/2}, \tag{14}$$

where μ is the coefficient of friction and

$$f(\nu) = 4.786\left(\frac{\nu^2\chi}{\chi^{-1}+3.2\nu+12.1824\nu^2\chi}\right)^{1/2} \tag{15}$$

Here χ is the radial distribution function given as (Ma & Ahmadi [7]),

$$\chi = \frac{1+2.5\nu+4.5904\nu^2+4.515439\nu^3}{\left[1-\left(\frac{\nu}{\nu_m}\right)^3\right]^{0.678021}}, \tag{16}$$

with ν_m =0.64356.

Earlier, using semi-empirical theories, several expressions for R were found. Ogawa *et al.* [4] reported

$$R = \sqrt{24\left(\frac{\nu}{\nu_m}\right)^{2/3}\frac{1-r}{1+r}}. \tag{17}$$

Ackermann & Shen [34] and Shen & Ackermann [31] obtained the following expression:

$$R = \sqrt{\left(\frac{\nu}{\nu_m}\right)^{1/3}\frac{1-r}{0.212}}, \tag{18}$$

while Jenkins & Savage [8] found

$$R = \sqrt{\frac{10}{3}(1-r)}. \tag{19}$$

The kinetic theory of and Lun *et al.* [10], led to a more complex expression for R. i.e.,

$$R = \left[\frac{1536}{5\pi}\frac{\eta(1-\eta)\nu^2 g_o(\nu)}{f(\nu,r)}\right]^{1/2}, \tag{20}$$

where

$$f(\nu,r) = \frac{1}{\eta(2-\eta)g_o(\nu)}(1+\frac{8}{5}\eta\nu g_o(\nu))\left[1+\frac{8}{5}\eta\nu g_o(\nu)(3\eta-2)\right]+\frac{768}{25\pi}\eta\nu^2 g_o(\nu), \tag{21}$$

$$g_o(\nu) = \frac{1}{1-\nu}+\frac{3\nu}{2(1-\nu)^2}+\frac{\nu^2}{2(1-\nu)^3}, \tag{22}$$

$$\eta = \frac{1}{2}(1+r). \tag{23}$$

Variation of Non-dimensional Normal Stress with R

In this section the variation of the experimentally determined kinetic normal stress, τ_{22}^k versus R is compared with the available model predictions for the normal stress for simple shear flows. From the experimental data, the kinetic stresses τ_{11}^k and τ_{22}^k were evaluated as

$$\hat{\tau}_{11} = \rho_p \nu u'^2 \quad and \quad \hat{\tau}_{22} = \rho_p \nu v'^2 \tag{24}$$

where ρ_p is the particle density and ν is the $3D$ solid volume fraction. These quantities were then non-dimensionalized by dividing by $\rho_p \nu^2 d^2 \dot{\gamma}^2$ as suggested by Lun *et al.* [10]. i.e.,

$$\hat{\tau}_{11} = \frac{\tau_{11}}{\rho_p \nu_{3D}^2 d^2 \dot{\gamma}^2} \quad and \quad \hat{\tau}_{22} = \frac{\tau_{22}}{\rho_p \nu_{3D}^2 d^2 \dot{\gamma}^2}. \tag{25}$$

The kinetic normal stress components for the present study were calculated using the experimentally determined section averaged RMS fluctuation energies u' and v',

while the predicted normal stress components for various models, which generally assume $\tau_{11} = \tau_{22}$, were dependent on the coefficient of restitution r and the solid volume fraction ν. The exception is the model of Abu-Zaid & Ahmadi [33] that includes the friction coefficient, i.e.,

$$\tau_{11} = \tau_{22} = 0.00728 f_1(\nu) \frac{2(1 + 4\nu\chi) + (R/f(\nu))}{\nu(R/f(\nu))}. \tag{26}$$

The normal stress components were also modeled by various authors in the past. The normal stress as found by Ogawa *et al.* [4] is given as

$$\tau_{11} = \tau_{22} = \frac{1}{8}\left(\frac{\nu}{1 - (\nu/\nu_m)^{1/3}}\right)\left(\frac{4r(3 + r)}{9R^2}\right). \tag{27}$$

Ackermann & Shen [34] and Shen and Ackermann [31] obtained the following expression

$$\tau_{11} = \tau_{22} = \frac{1}{8}\left(\frac{\nu(\nu/\nu_m)^{1/3}}{1 - (\nu/\nu_m)^{1/3}}\right)\left(\frac{8\sqrt{2}(1 + r)}{\pi^2 R^2}\right), \tag{28}$$

while Jenkins and Savage [8] found

$$\tau_{11} = \tau_{22} = \frac{4\nu^2 g_o(\nu)}{3R^2}. \tag{29}$$

The theory of Lun *et al.* [10] led to

$$\tau_{11} = \tau_{22} = \frac{4}{3R^2} + \frac{6(4 + \pi)}{35\pi} - \frac{6(4 - \pi)}{35\pi}\left[\frac{R^2}{R^2 + \sqrt{858(4 - \pi)}}\right] \tag{30}$$

Comparison of Root-Mean-Square Velocities with the Model of Abu-Zaid & Ahmadi

In this appendix the root-mean-square velocities as predicted by the model of Abu-Zaid & Ahmadi [33] is described. Using a thermodynamic basis, Abu-Zaid & Ahmadi developed an anisotropic rate-dependent model for granular flows which accounts for the non-isotropic fluctuation velocity components during rapid granular flows. The corresponding root-mean-square velocity components may be evaluated as

$$u' = \sqrt{-\left(\frac{\tau_{11}^k}{\rho}\right)} \quad and \quad v' = \sqrt{-\left(\frac{\tau_{22}^k}{\rho}\right)} \tag{31}$$

where τ_{11}^k and τ_{22}^k are the normal kinetic stresses given by

$$\tau_{11}^k = -p^{Tk} - \rho k T^2 \left(\frac{\alpha}{2} + \frac{\beta}{12}\right)\dot{\gamma}^2 \quad and \quad \tau_{22}^k = -p^{Tk} + \rho k T^2 \left(\frac{\alpha}{2} + \frac{\beta}{12}\right)\dot{\gamma}^2. \tag{32}$$

Here, the mass density ρ is the product of the particle density $\rho_o = 2.947 gm/cm^3$ (for glass) and the solid volume fraction $\overline{\nu}_{3D}$. i.e.,

$$\rho = \rho_o \nu. \tag{33}$$

In equation (32), p^{Tk} is the kinetic part of the granular pressure defined as

$$p^{Tk} = \frac{2}{3}\rho k, \tag{34}$$

and T is the time scale of granular fluctuation given by

$$T = \frac{1}{ak^{1/2}}. \tag{35}$$

The material parameters α, β, and ζ are given as

$$\alpha = \frac{1}{2}(1-r^2)^{2.25}, \quad \beta = \frac{3}{4}(1-r^2)^{2.25}, \quad and \quad \zeta = \frac{\beta^2}{48\hat{C}^\mu}, \tag{36}$$

and

$$a = \alpha_o(1-r^2)\frac{\nu\chi}{d}, \tag{37}$$

where χ is the radial distribution function.

The fluctuation kinetic energy for the simple shear flow of granular materials in grain inertia regime is given by

$$k = \frac{C^\mu d\dot{\gamma}^2}{2a}\left(1+\sqrt{1+\frac{\zeta}{\hat{C}^\mu C^\mu a d}}\right), \tag{38}$$

where

$$C^\mu = 0.0754\frac{f(\nu,r)}{\nu}, \tag{39}$$

with

$$f(\nu,r) = \frac{4}{\chi(3-r)(r+1)}\left[1+\frac{4}{5}(1+r)\nu\chi\right]\left[1+\frac{2}{5}(r+1)(3r-1)\nu\chi\right]+\frac{384}{25\pi}(1+r)\nu^2\chi. \tag{40}$$

In equations (36) and (38), $\hat{C}^\mu$ is a positive function given by

$$\hat{C}^{\mu} = \alpha_o C^{\mu} \nu \chi (1 - r^2), \tag{41}$$

where $\alpha_o = 3.685$ is a constant.

APPENDIX C List of Symbols

a	Material Parameter
α	Material Parameter
α_o	Constant
A_p	Circumferential Area of Particle
A_{pack}	Packing Area
$\mathcal{A}$	Surface Area for Determination of Solids Fraction
β	Material Parameter
$\dot{\gamma}$	Effective Shear-Rate
$\dot{\gamma}^I$	Ideal Shear-Rate
C^{μ}	Function of ν and r
$\hat{C}^{\mu}$	Positive Function of ν and Physical Properties of Granules
d	Particle Diameter
ζ	Function of β and $\hat{C}^{\mu}$
η	Function of r
$f(\nu, r)$	Function of χ and ν
$g_o(\nu)$	Distribution Function
H	Width of Annulus
k	Fluctuation Kinetic Energy for the Mean Granular Motion in Grain Inertia Regime
MPF	Maximum Packing Factor
μ	Coefficient of Friction
N_f	Number of Frames Analyzed per Flow
N_p	Number of Particles Within a Bin
N_{total}	Total Number of Particles Mapped

p^T	Granular Pressure
r	Coefficient of Restitution
ρ	Mass Density
ρ_o	Material Density
RMS	Root-Mean-Square Velocity
rpm	Revolutions per Minute
R	Scaled Shear to Velocity Ratio
s_{2D}	Linear Concentration Parameter in 2D
s_{3D}	Linear Concentration Parameter in 3D
S	Width Between Roughened Wall Bumps
σ	Roughened Wall Bump Diameter
T	Time Scale of Granular Fluctuation
τ_{11}	Normal Stress
τ_{22}	Normal Stress
τ_{11}^k	Kinetic Stress
τ_{22}^k	Kinetic Stress
$U^{(i)}$	Velocity of Particle in x-Direction
$u'^{(i)}$	x Component of RMS-Velocity
u_{inner}	Velocity of Inner Wall
u_{outer}	Velocity of Outer Wall
u_{slip}	Slip Velocity
u_{wall}	General Wall Velocity
$V^{(i)}$	Velocity of Particle in Transverse Direction
$\mathcal{V}$	Volume of Test-Section for Determination of Solids Fraction
$v'^{(i)}$	y Component of RMS-Velocity
V_θ	θ Velocity of Particle
v'_θ	θ Component of RMS-Velocity
V_r	Radial Component of Velocity
v'_r	Radial Component of RMS-Velocity
$\overline{\nu}_{2D}$	Average Surface Fraction

$\overline{\nu}_{3D}$	Average Solid Volume Fraction
ν_{2DM}	Maximum Solids Packing Factor in 2D
ν_{3DM}	Maximum Solids Packing Factor in 3D
ν_m	Maximum Solids Packing Factor for Shear
$x_j^{(i)}$	Particle Coordinate
χ	Radial Distribution Function
$y_j^{(i)}$	Particle Coordinate

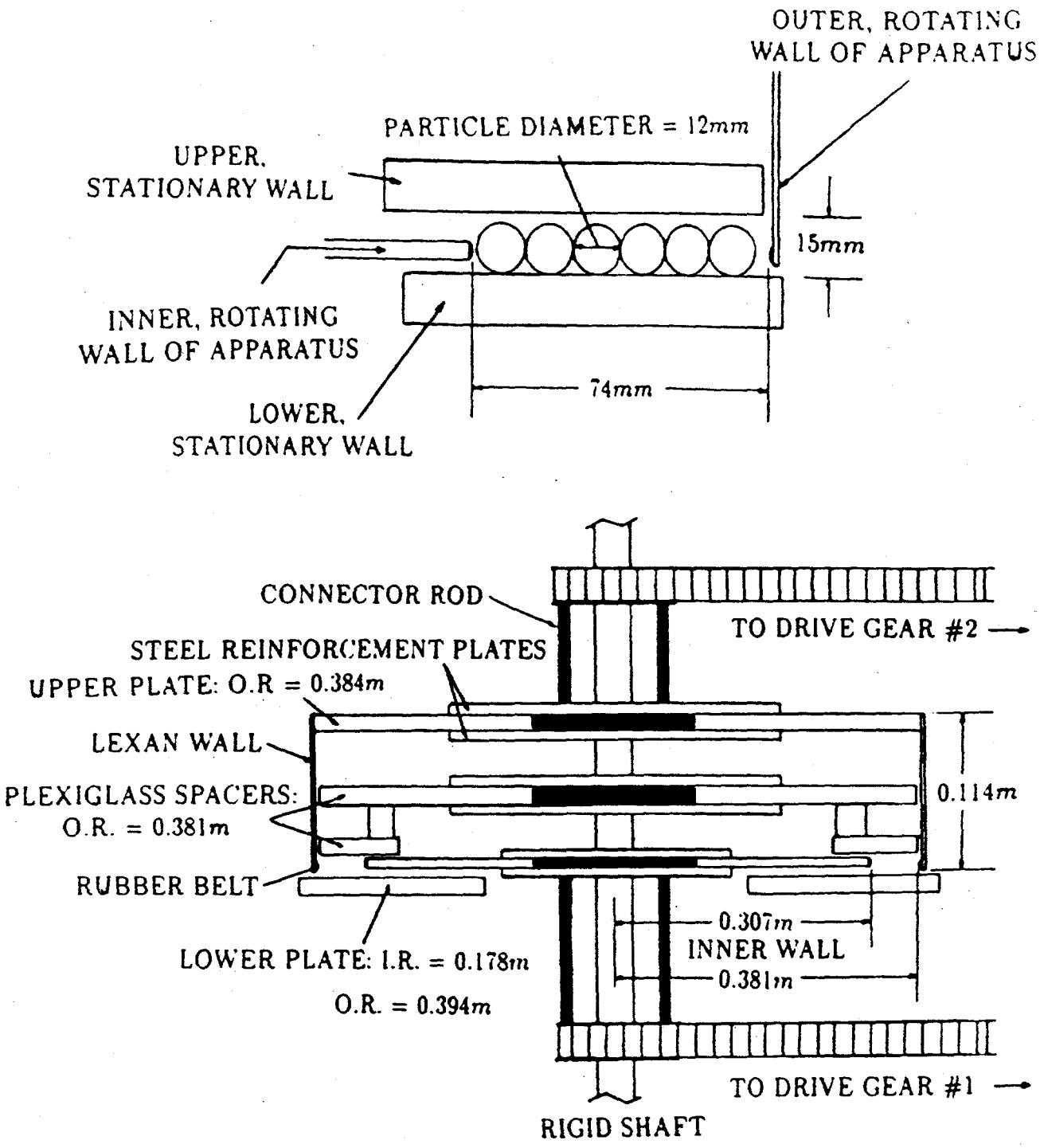

Figure 1: Schematic of the Experimental Setup.

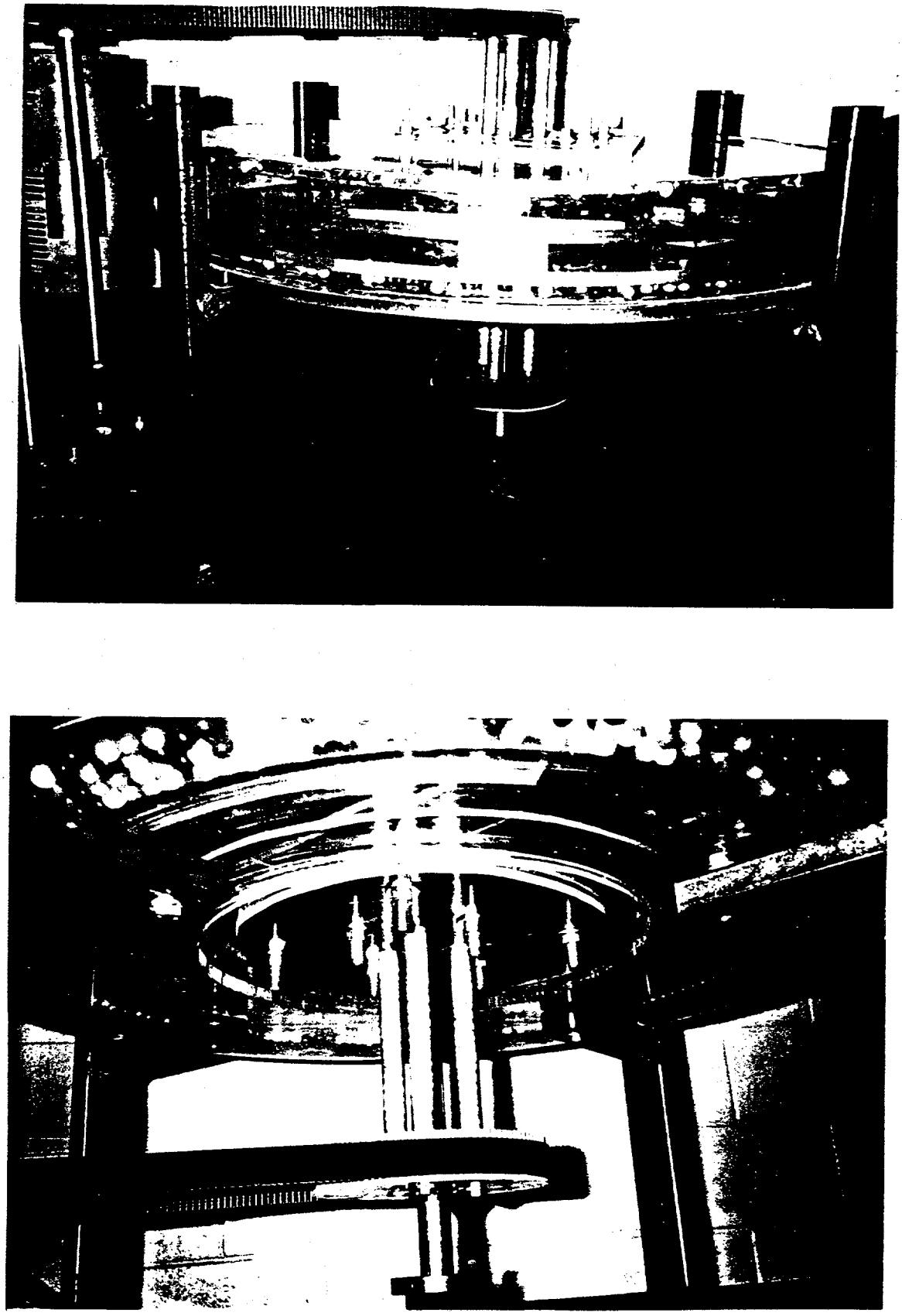

Figure 2: Photograph of the Experimental Facility.

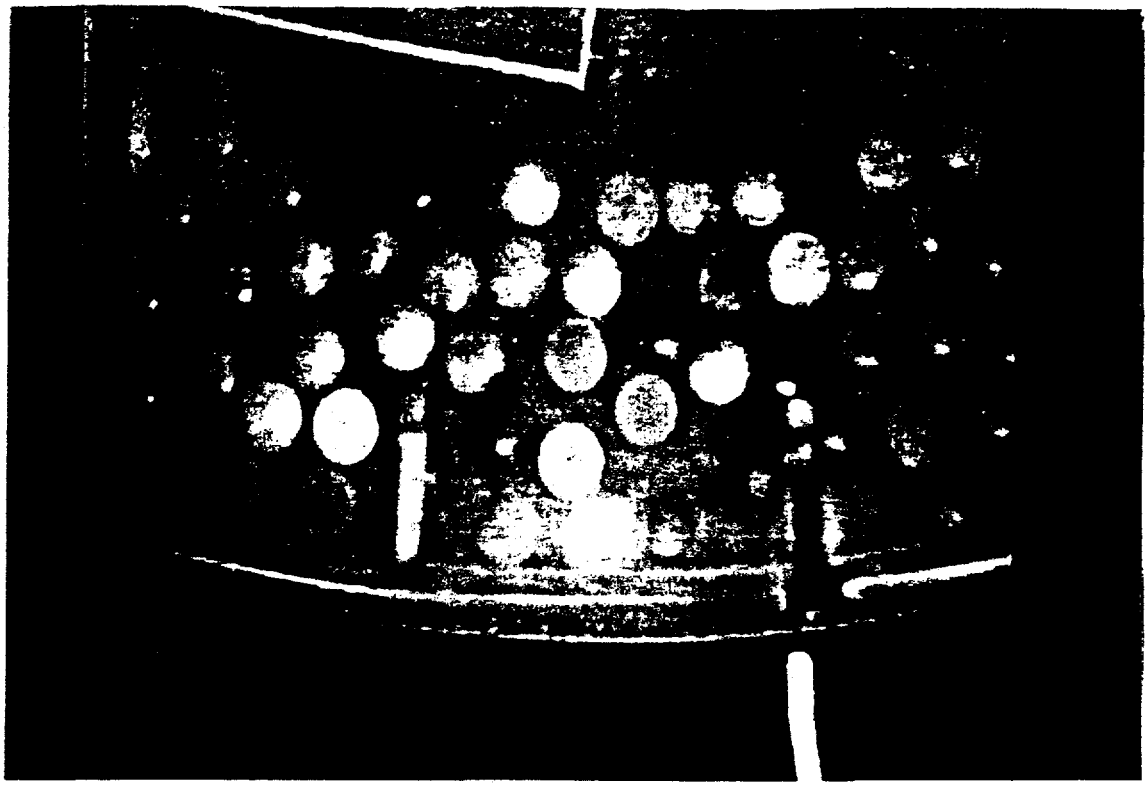

Figure 3.3: Photograph 1 of one Frame at $\overline{v}_{2D} = 23\%$ and 60 *rpm*

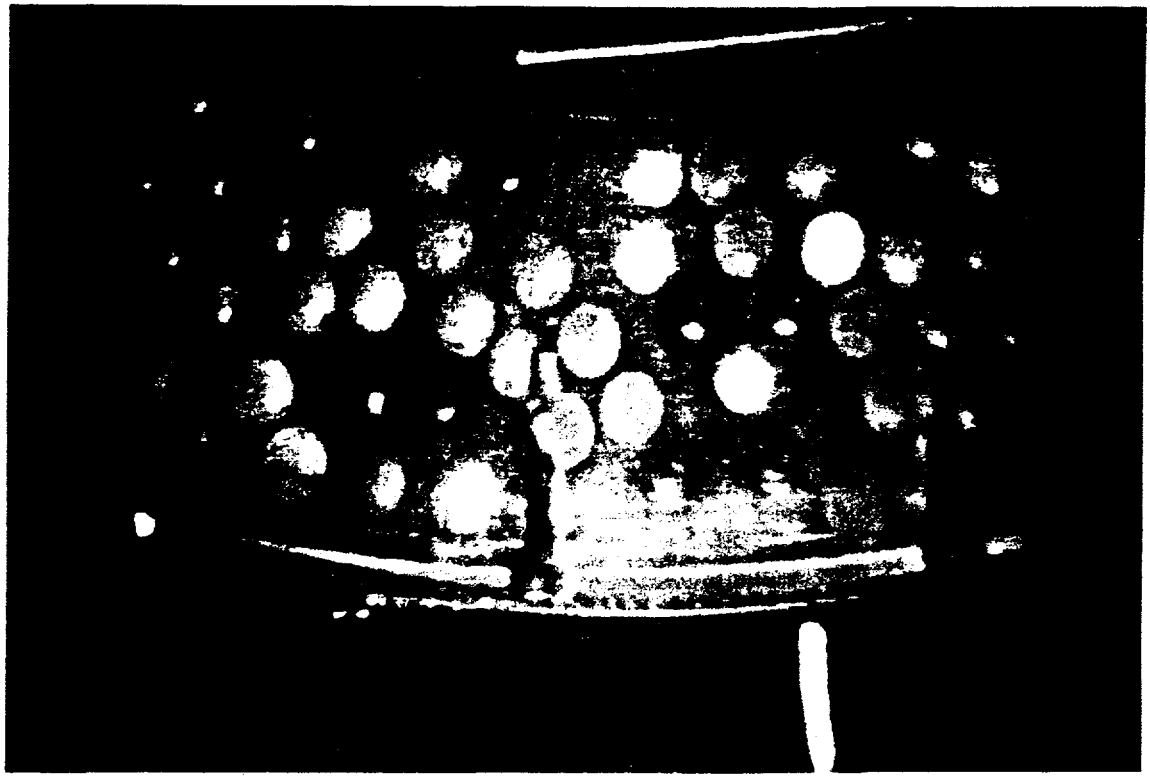

Figure 3: Photographs of Two Consecutive Frames at $\overline{v}_{2D} = 23\%$ and 60 *rpm*

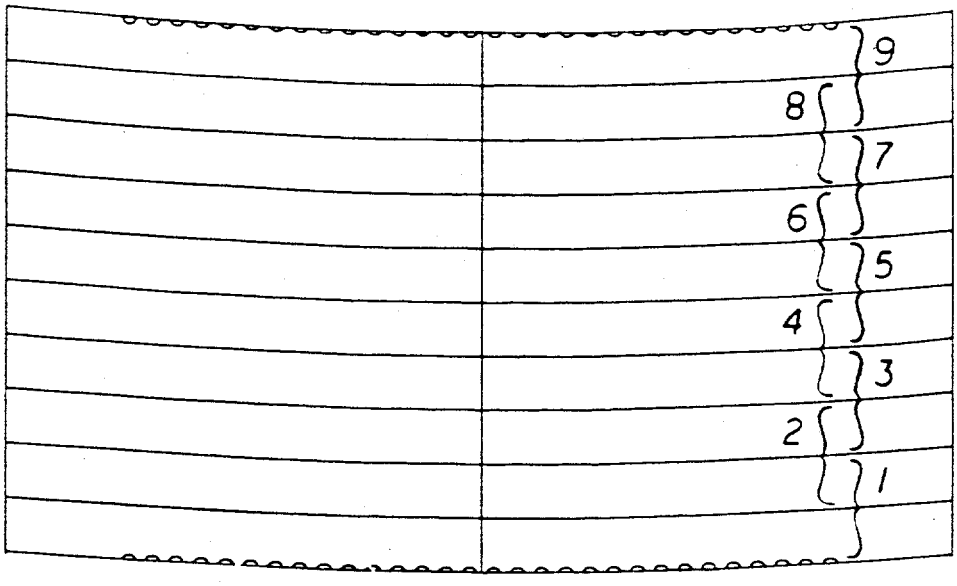

Figure 4: Schematic of Overlapping Bins

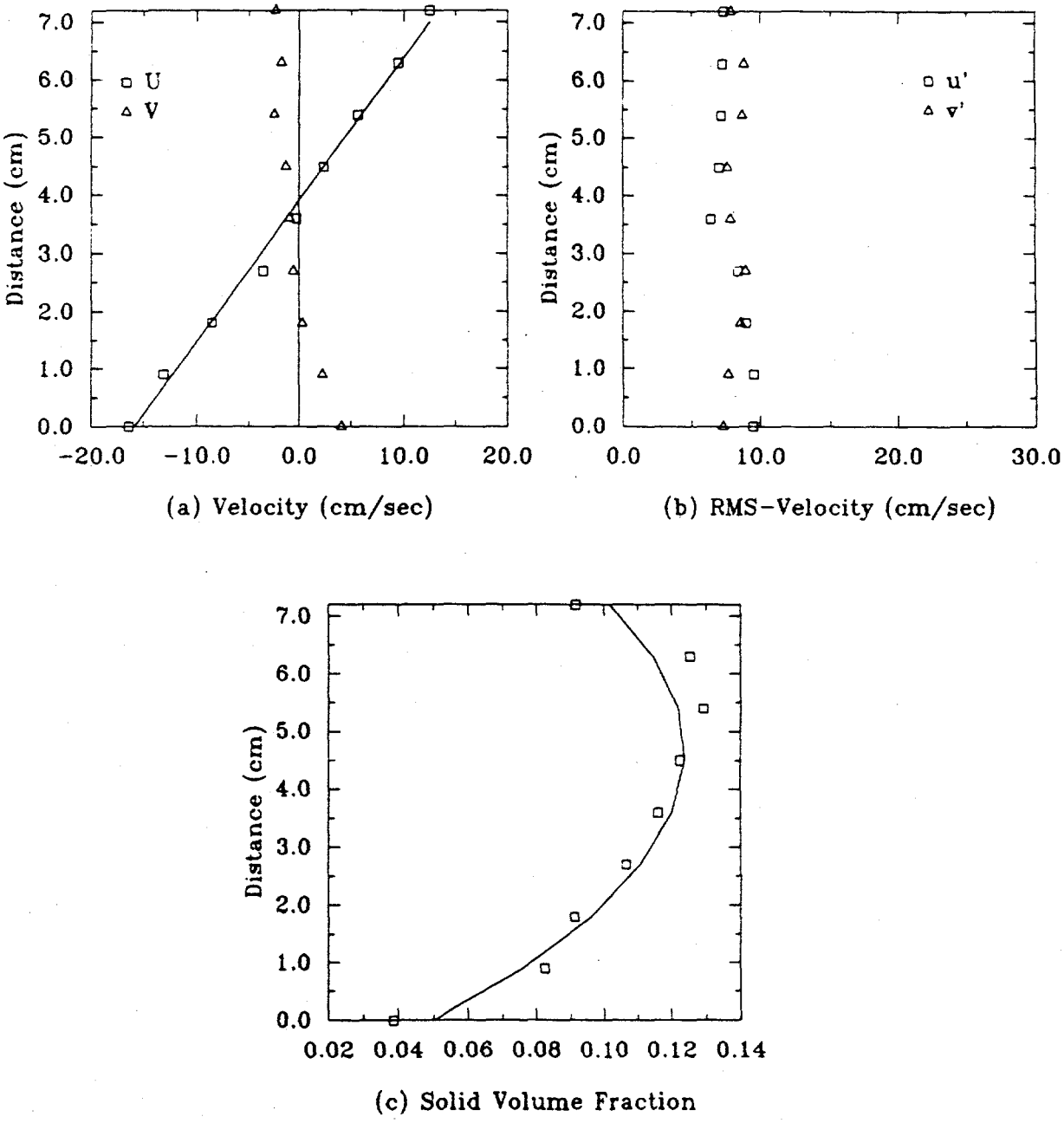

Figure 5: Variations of mean and fluctuation velocities and solid volume fraction for $\overline{v}_{3D} = 9.8\%$ and $\dot{\gamma} = 4\ sec^{-1}$

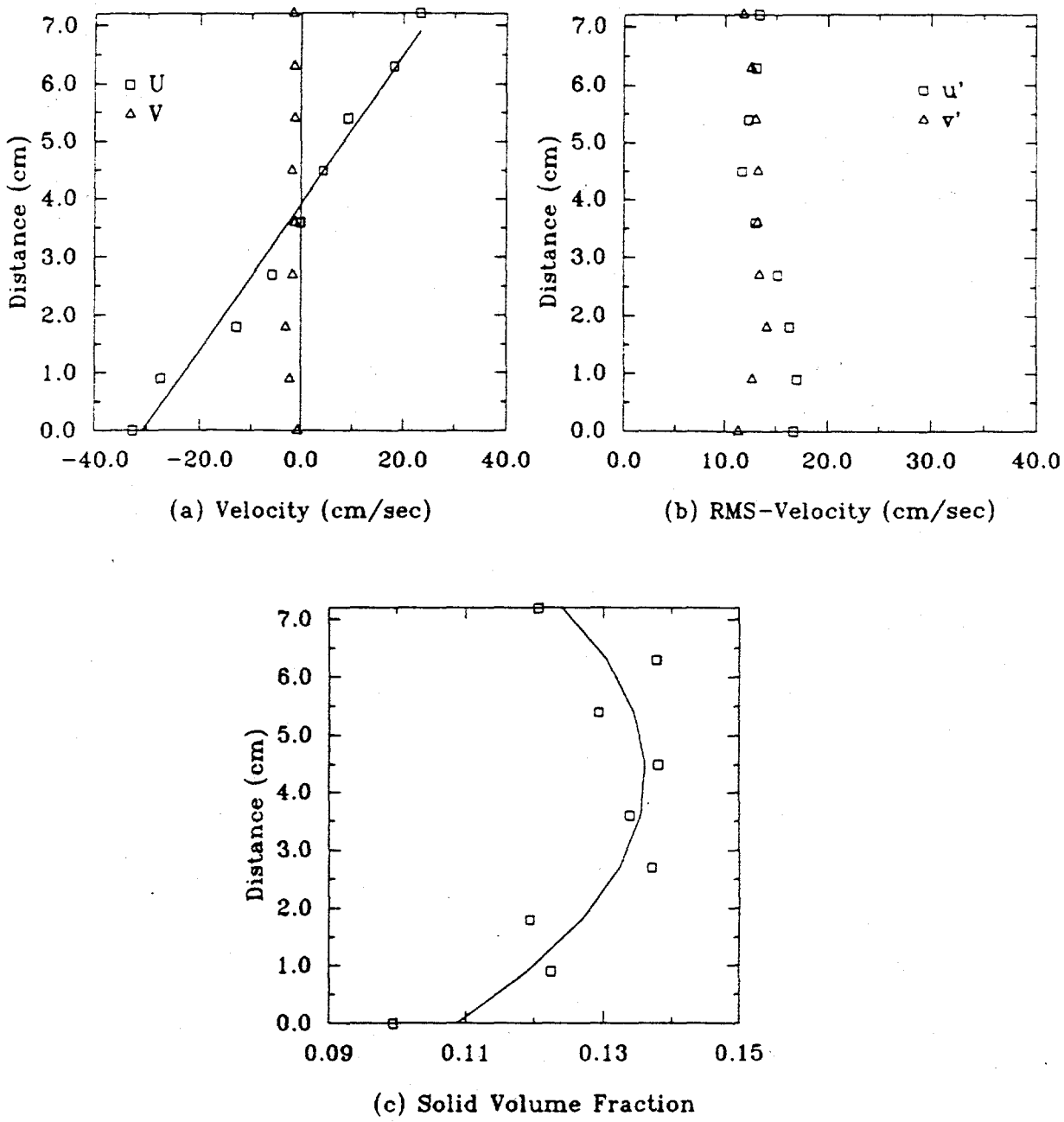

Figure 6: Variations of mean and fluctuation velocities and solid volume fraction for $\overline{\nu}_{3D} = 12.6\%$ and $\dot{\gamma} = 7.9\ sec^{-1}$

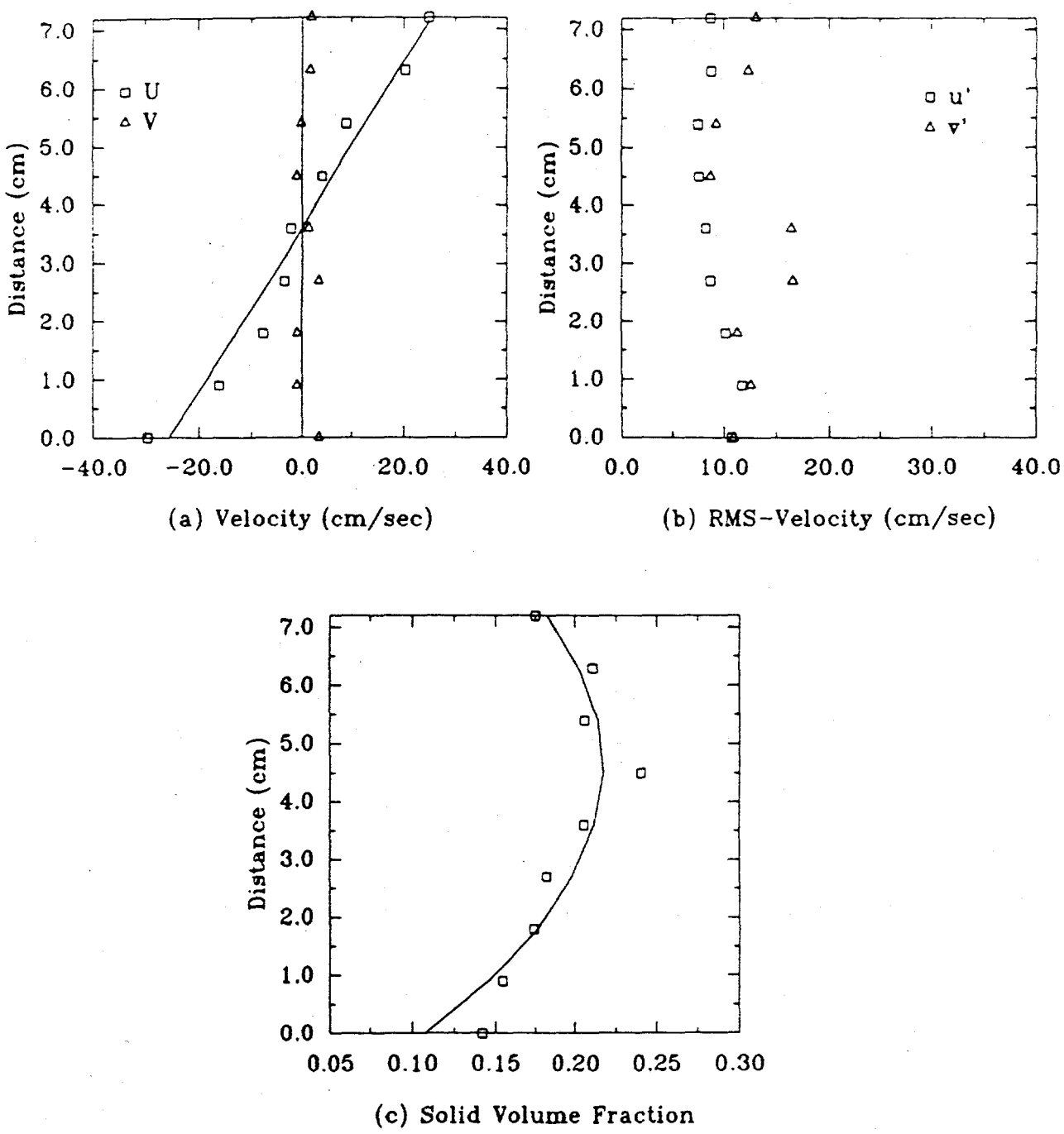

Figure 7: Variations of mean and fluctuation velocities and solid volume fraction for $\overline{\nu}_{3D} = 19.7\%$ and $\dot{\gamma} = 6.9\ sec^{-1}$

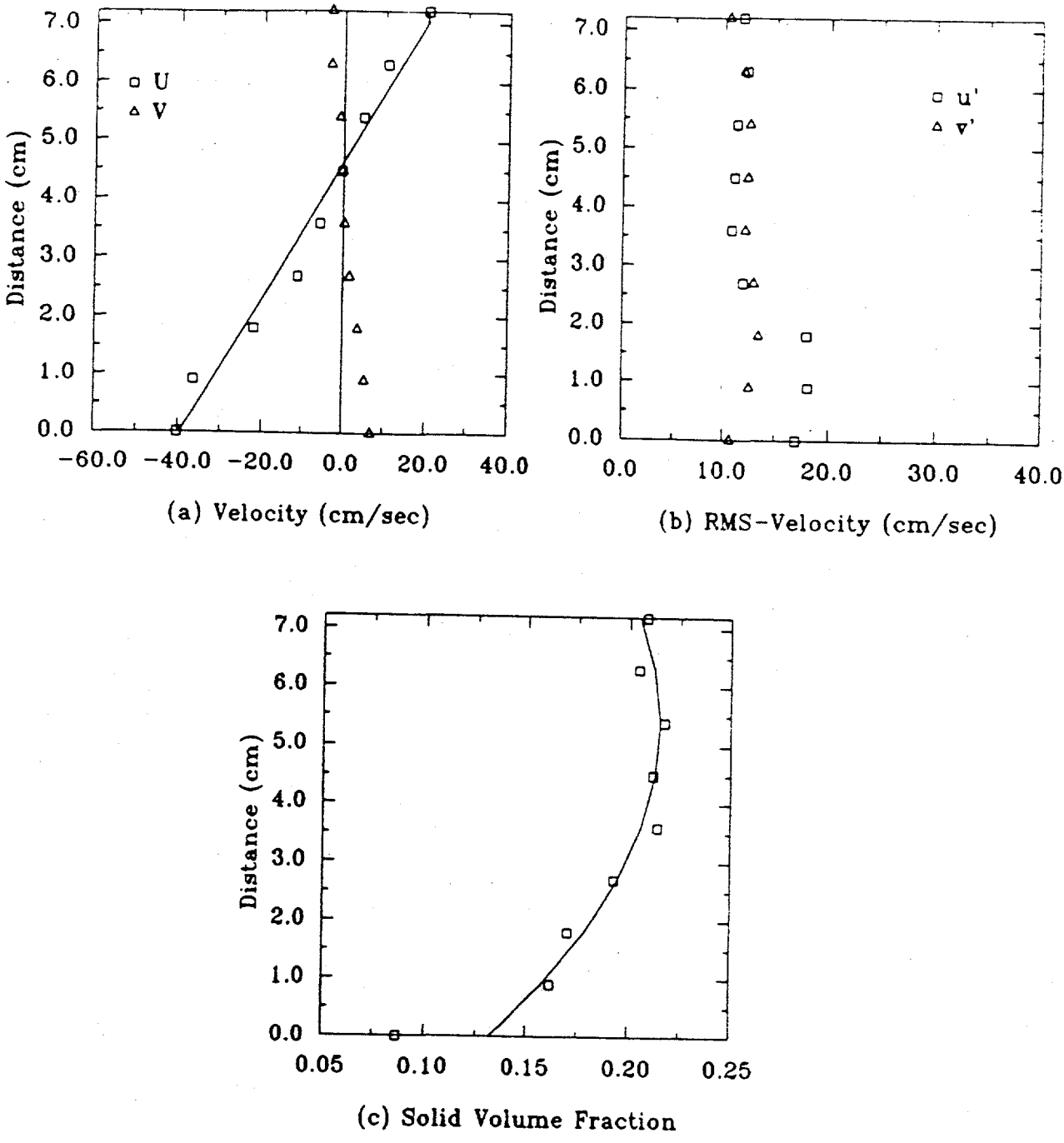

Figure 8: Variations of mean and fluctuation velocities and solid volume fraction for $\overline{\nu}_{3D} = 19.7\%$ and $\dot{\gamma} = 8.8\ sec^{-1}$

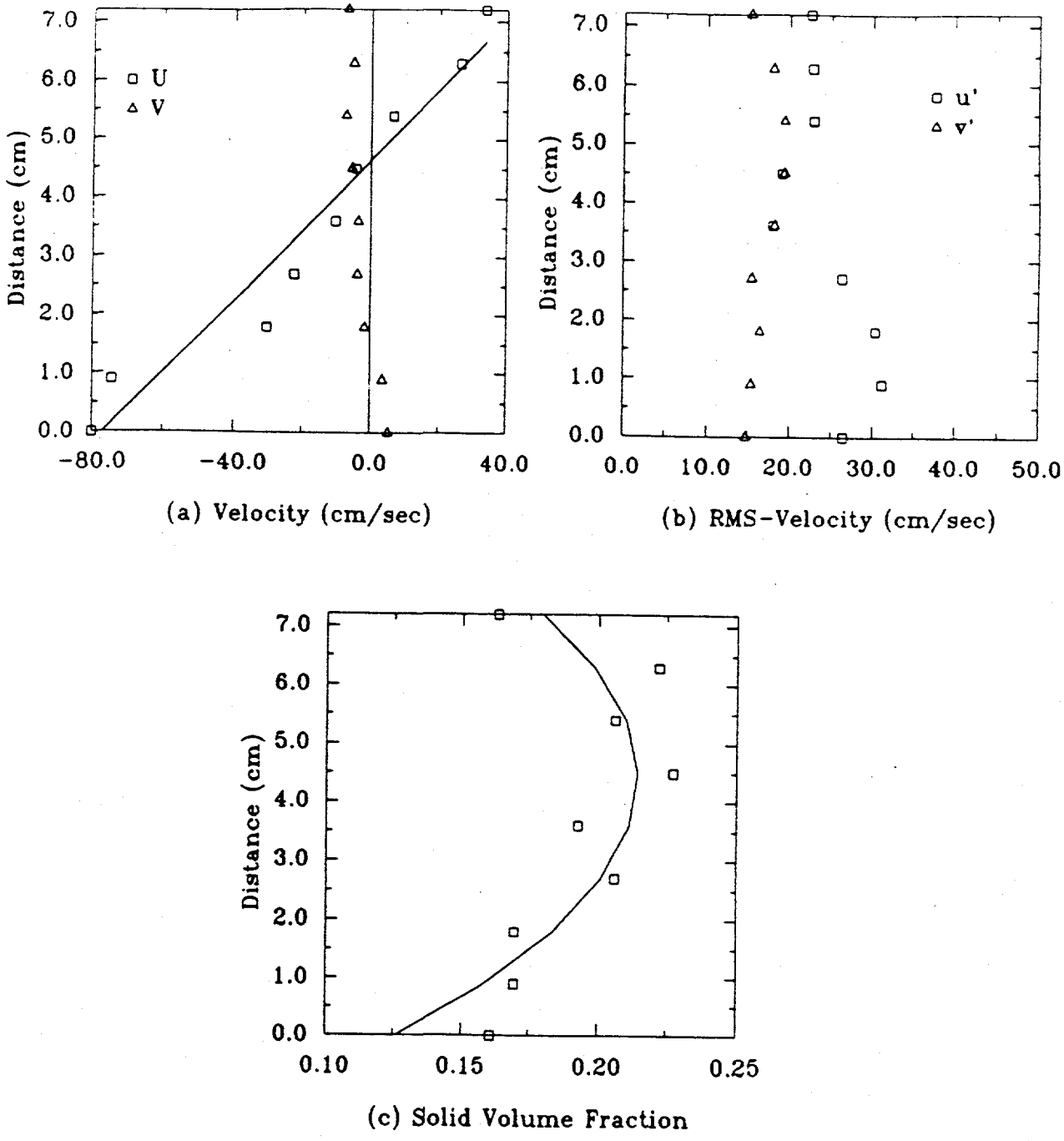

Figure 9: Variations of mean and fluctuation velocities and solid volume fraction for $\overline{\nu}_{3D} = 19.7\%$ and $\dot{\gamma} = 15.6\ sec^{-1}$

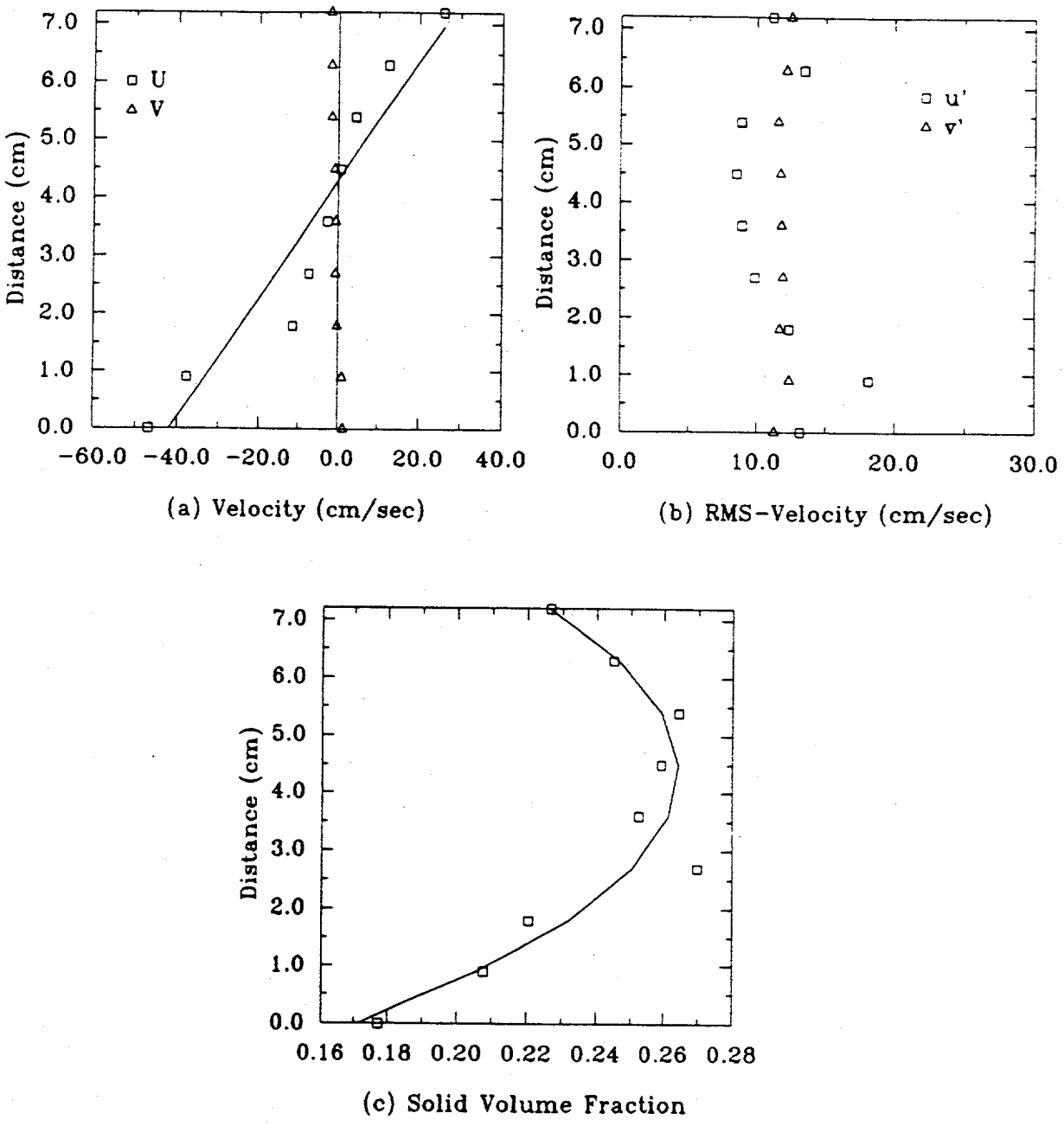

Figure 10: Variations of mean and fluctuation velocities and solid volume fraction for $\overline{\nu}_{3D} = 25.1\%$ and $\dot{\gamma} = 10\ sec^{-1}$

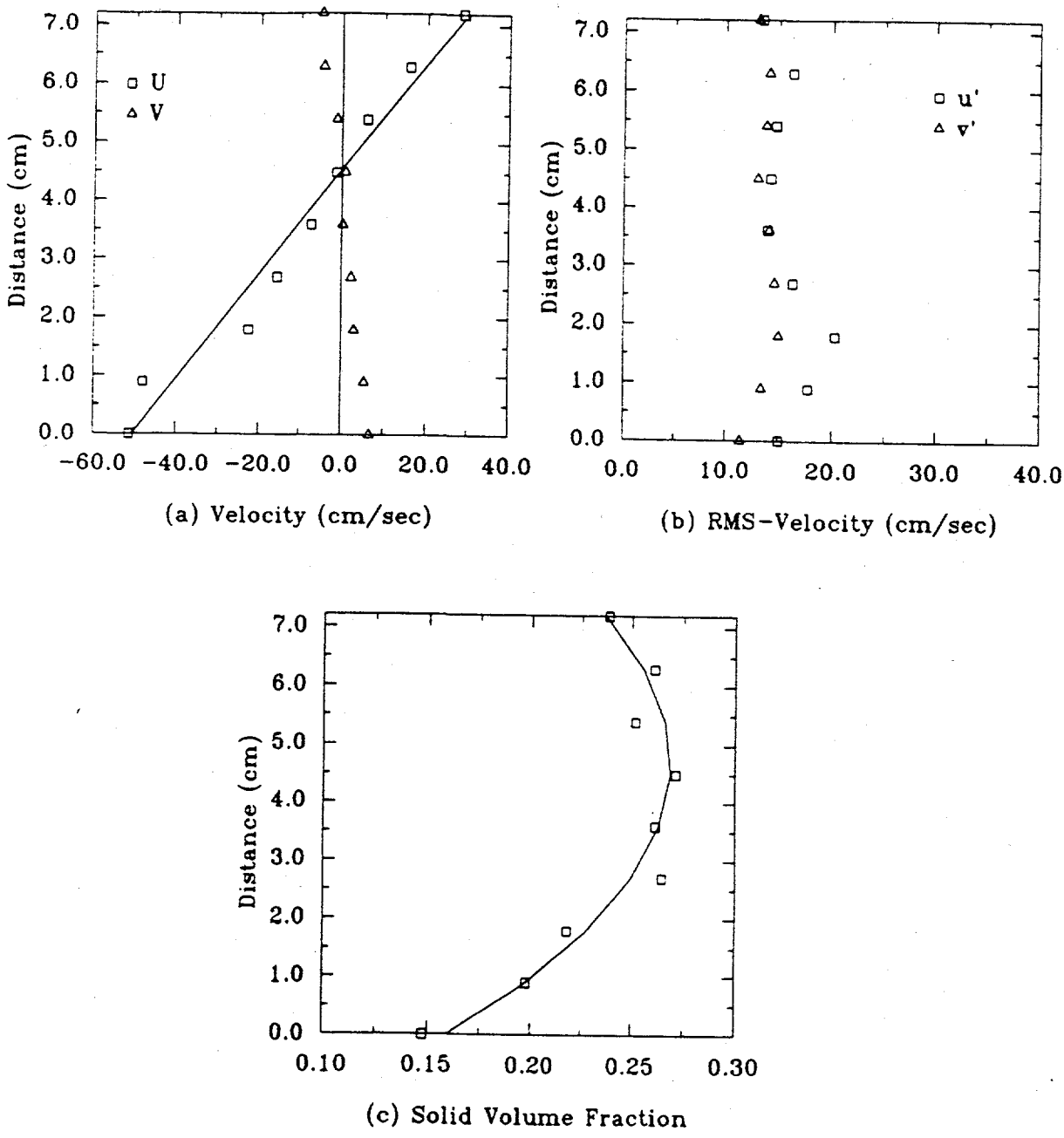

Figure 11: Variations of mean and fluctuation velocities and solid volume fraction for $\overline{\nu}_{3D} = 25.1\%$ and $\dot{\gamma} = 11.5\ sec^{-1}$

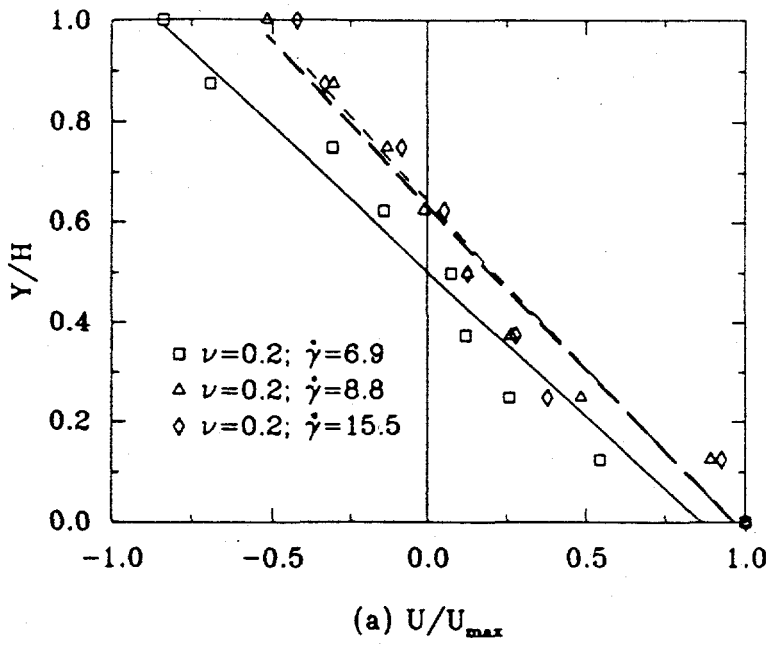

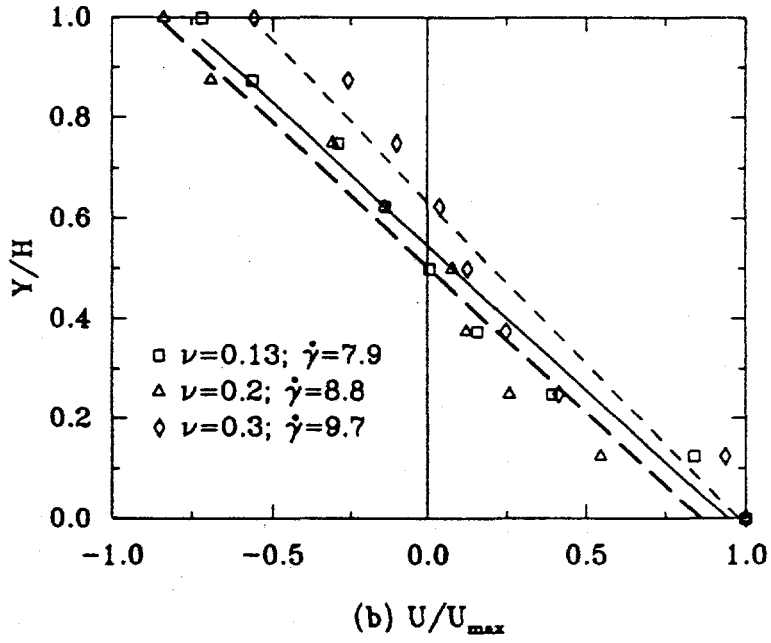

Figure 12: Variations of non-dimensional mean velocity across the annulus

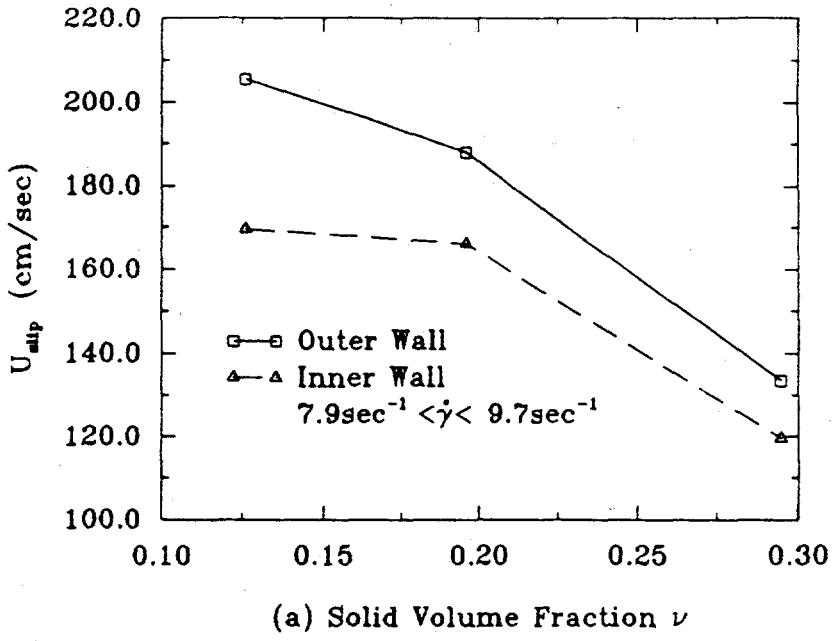

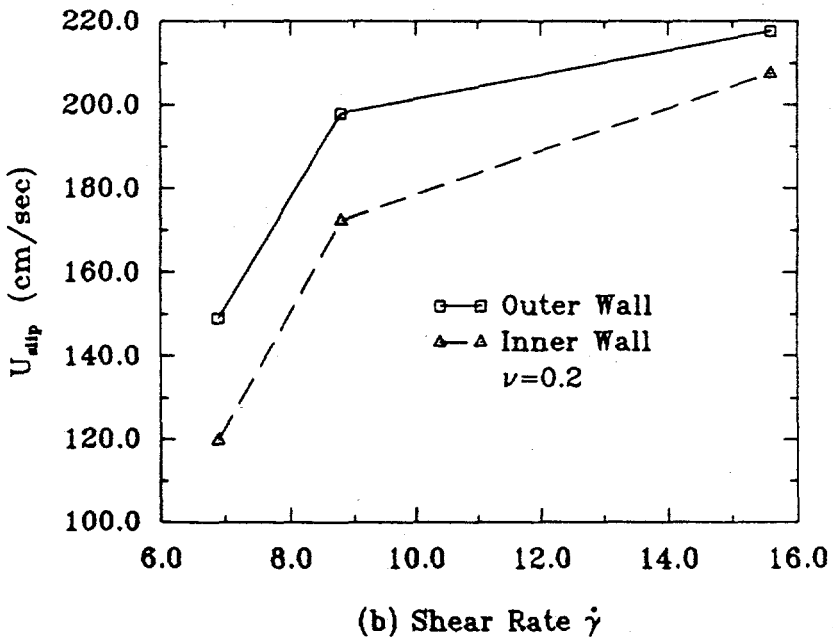

Figure 13: Variations of slip velocity with solid volume fraction and shear rate

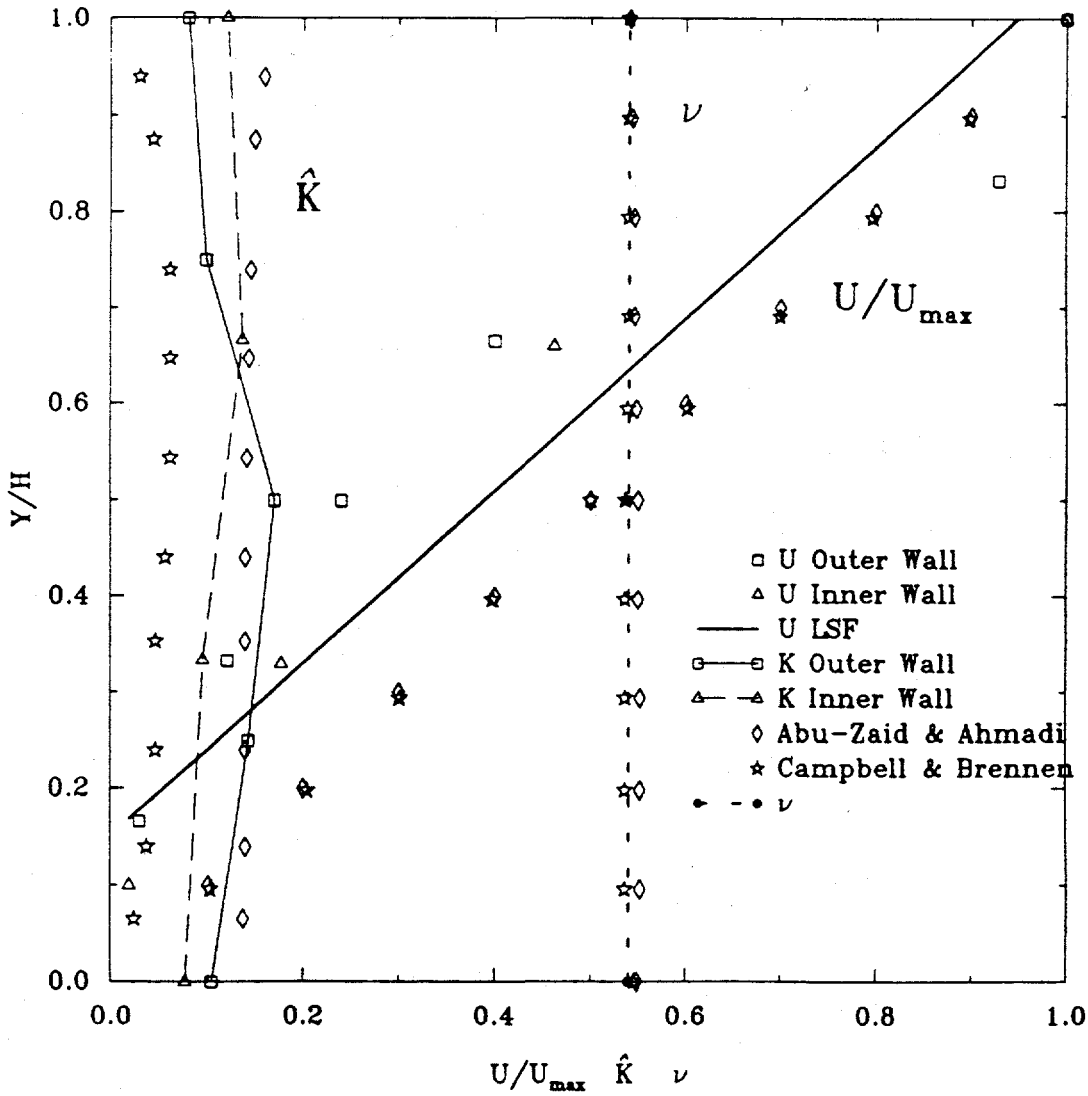

Figure 14: Comparisons of non-dimensional U/U_{max} velocity and fluctuation kinetic energy for $\overline{\nu}_{2D}$=0.54

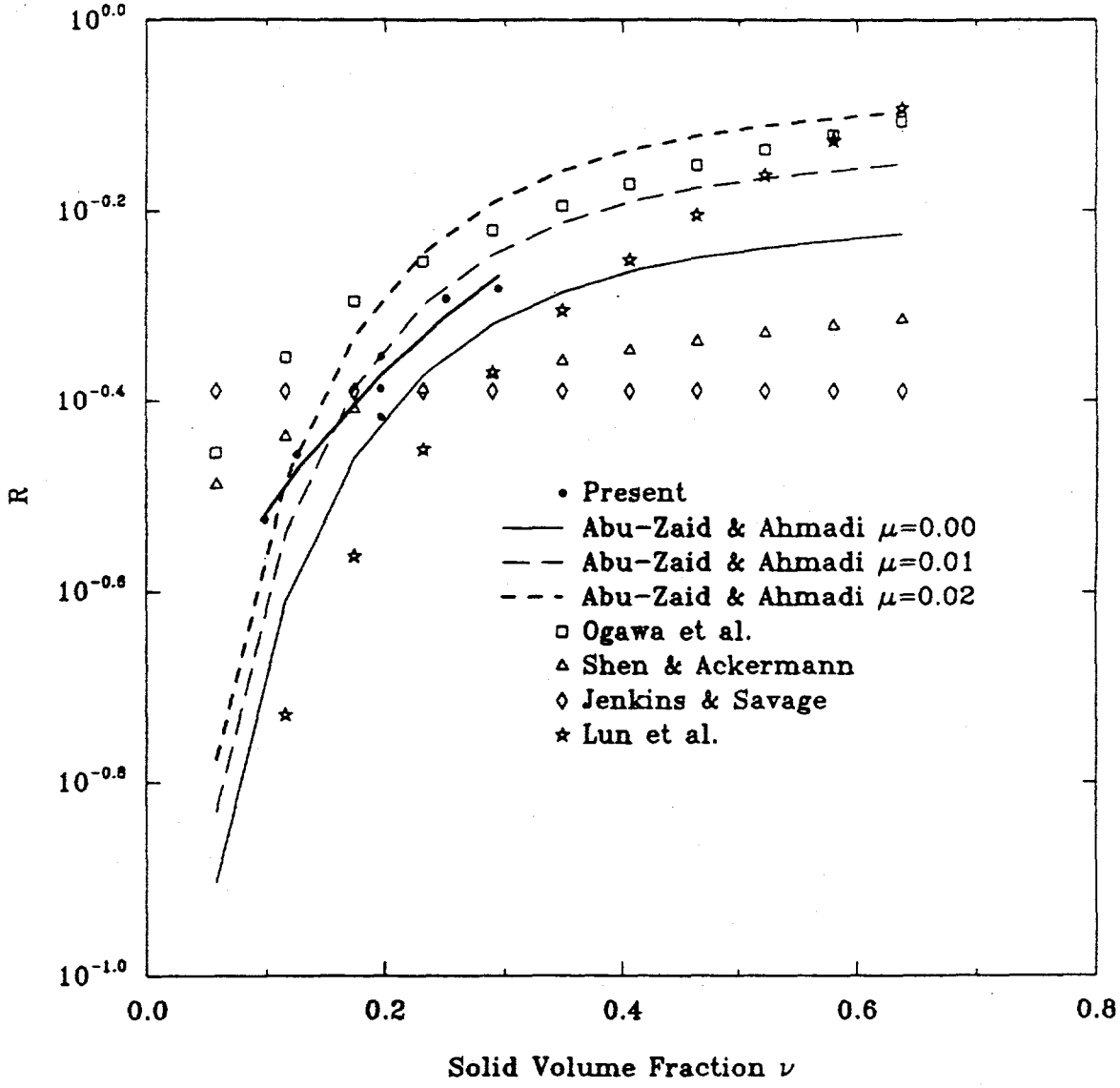

Figure 15: Variation of mean shear rate to fluctuation energy ratio R with solid volume fraction

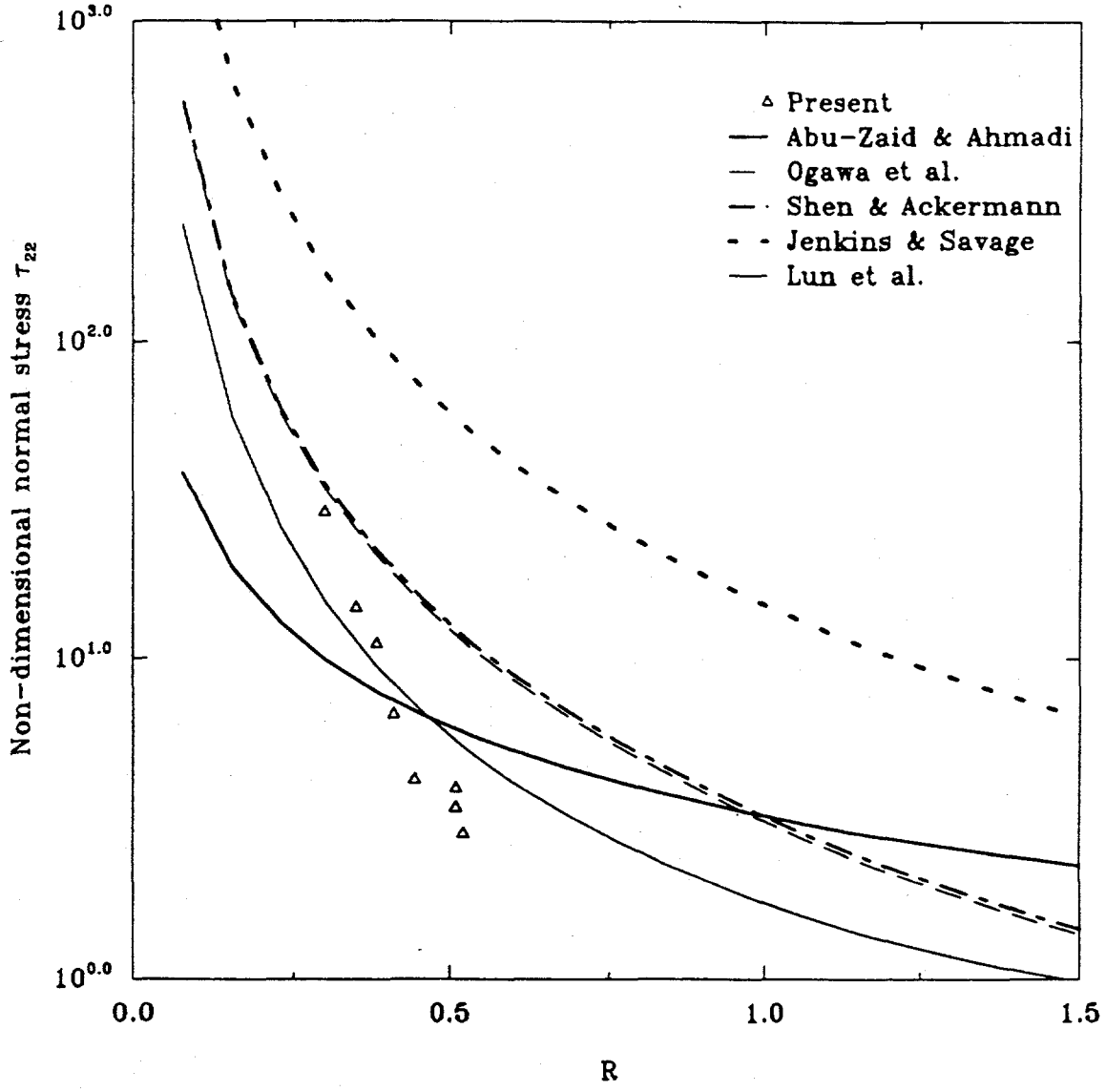

Figure 16: Variation of non-dimensional normal stress component with the ratio of characteristic mean shear velocity R

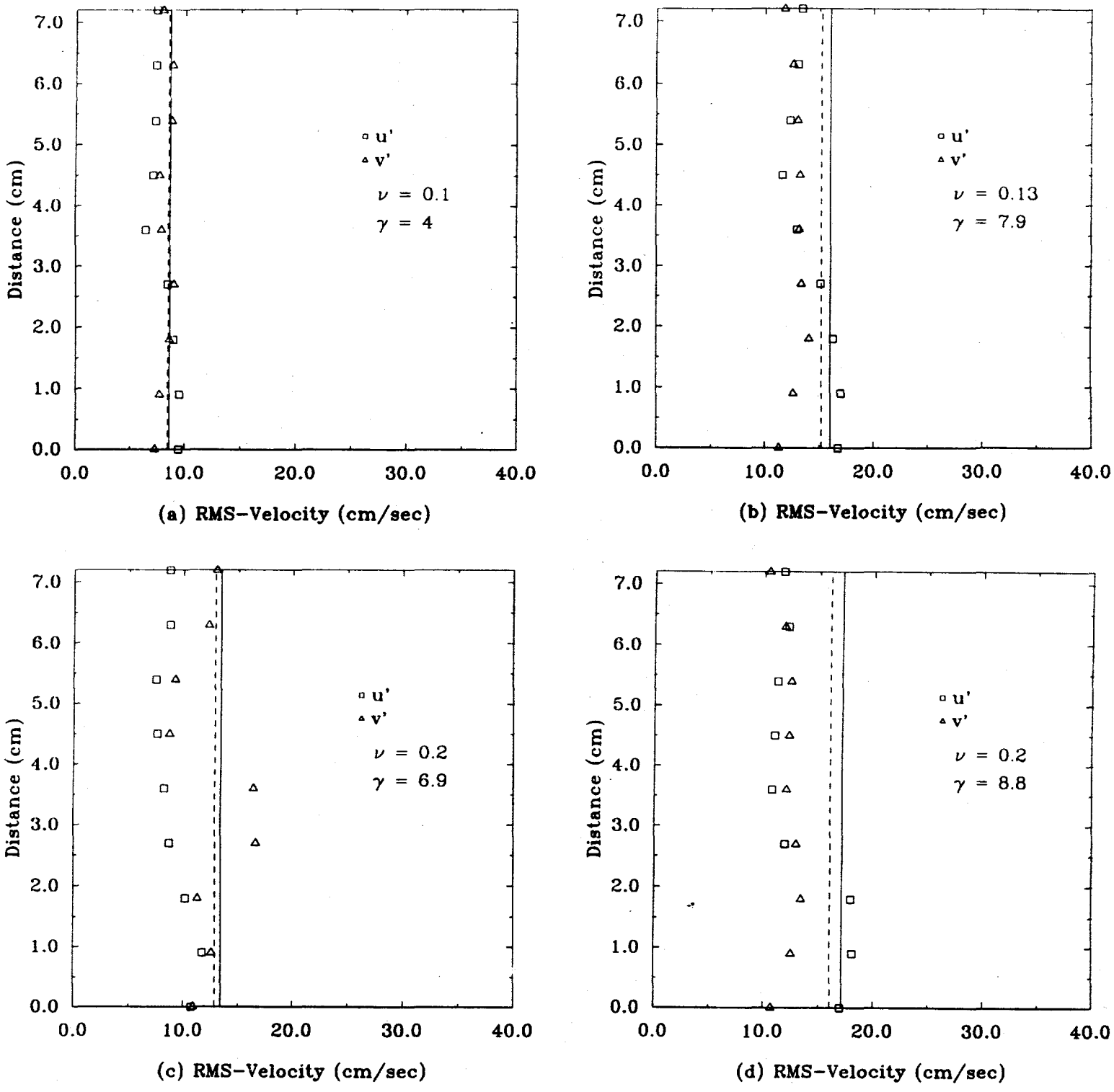

Figure 17: Comparison of root-mean-square velocities for Shear rates in the range of 4 to 8.8 sec^{-1}

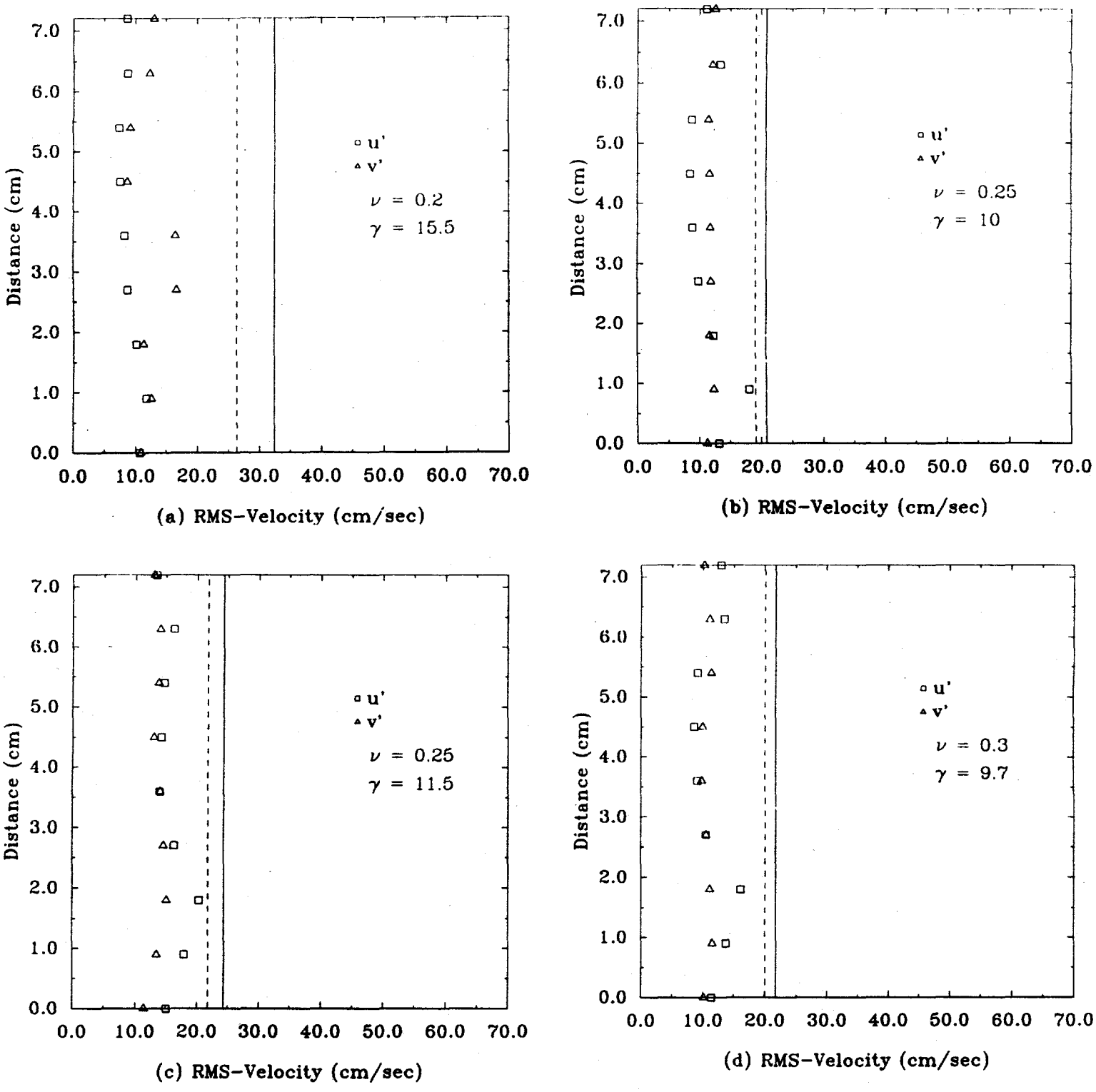

Figure 18: Comparison of root-mean-square velocities for Shear Rates in the range of 9.7 to 15.6 sec^{-1}